Journal of Drug Delivery Science and Technology 125 (2026) 108673

Contents lists available at ScienceDirect

Journal of Drug Delivery Science and Technology

journal homepage: www.elsevier.com/locate/jddst

Development of a next-generation wound-healing scaffold integrating decellularized dermis with tailored mesenchymal stromal cell secretomes

Marta Cecilia Tosca [a,1], Simona Turi [b,c,1], Dmitry Lim [d], Angelo Modena [d], Edoardo Bertania [d], Elia Bari [d,*], Lorena Segale [d], Lorella Giovannelli [d], Ivana Miletto [d], Ilenia Rita Renzulli [e], Rossana Rossi [b], Pierluigi Mauri [b], Dario Di Silvestre [b], Giovanni Sesana [a,1], Maria Luisa Torre [d,f,1]

[a] Grande Ospedale Metropolitano Niguarda, Piazza Ospedale Maggiore 3, Milano, 20162, Italy
[b] Institute for Biomedical Technologies-National Research Council, Department of Biomedical Sciences, Via F.lli Cervi 93, Segrate, 20054, Italy
[c] Department of Biomedical Sciences, University of Padova, Via Ugo Bassi 58/B, Padova, 35131, Italy
[d] Department of Pharmaceutical Sciences, University of Piemonte Orientale, Largo Donegani 2/3, Novara, 28100, Italy
[e] Department of Civil Engineering and Architecture, University of Pavia, Via Ferrata 3, Pavia, 27100, Italy
[f] PharmaExceed s.r.l., Piazza Castello 19, Pavia, 27100, Italy

ARTICLE INFO

Keywords:
Chronic wounds
Decellularized dermis
Mesenchymal stromal cells
MSC-secretome
Wound healing
Tissue regeneration

ABSTRACT

Chronic wounds are difficult to treat due to impaired cell proliferation, persistent inflammation, and delayed tissue remodeling. To address these challenges, biologically active scaffolds were developed by combining human decellularized dermis, obtained from cadaveric donors, with a standardized, freeze-dried secretome derived from mesenchymal stromal cells (MSC). Dermis scaffolds were prepared using five decellularization protocols, resulting in acellular matrices (DNA content <50 ng/mg) that preserved the extracellular matrix (ECM) architecture. These matrices were subsequently loaded with secretomes isolated from MSCs that were serum-starved alone or in combination with IL-1β or hypoxia. In vitro wound-healing assays demonstrated that secretomes from serum-starved and IL-1β-primed cells accelerated fibroblast and human umbilical vein endothelial cells closure (e.g., IL-1β-primed secretomes significantly reduced fibroblast wound area as early as 16 h, versus 45.1% residual wound area in untreated controls at 48 h), whereas secretomes derived from hypoxic conditions had a minimal effect. These differences correlated with the proteomic composition of MSC-secretomes (1051 proteins identified overall, 26% shared across all three conditions): IL-1β enhanced matrix remodeling and wound repair proteins, serum starvation enriched ECM components, and hypoxia favored cytoprotective proteins. Together, these results demonstrate that combining tailored MSC-secretomes with decellularized dermis provides a ready-to-use, off-the-shelf system capable of overcoming multiple barriers in chronic wound healing, offering a promising strategy for regenerative therapy.

1. Introduction

Chronic wounds remain a major public health burden, affecting approximately 10.5 million people in the United States (US) alone [1] and showing a prevalence of 1-2% in European countries [2]. The problem is especially prominent among aging populations, where underlying chronic conditions, such as diabetes and vascular diseases, are prevalent contributors [3,4]. As a result, the economic burden is also significant, with healthcare costs for chronic wound care projected to reach up to $90 billion annually in the US alone [5,6].

Chronic wounds are marked by impaired healing – defined as less than 30% wound closure after 4-12 weeks [7] – due to the disrupted cellular and molecular signaling during the inflammatory, proliferative, and remodeling phases. Persistent inflammation, characterized by elevated levels of pro-inflammatory cytokines, reactive oxygen species, and proteases, prevents the transition from the inflammatory to the proliferative phase, thereby hampering tissue repair and regeneration and destroying both the old and newly synthesized extracellular matrix

* Corresponding author.
E-mail address: elia.bari@uniupo.it (E. Bari).
[1] Equally contributed.

https://doi.org/10.1016/j.jddst.2026.108673
Received 27 May 2026; Received in revised form 1 July 2026; Accepted 2 July 2026
Available online 3 July 2026

(ECM) [8]. Bacterial infections further complicate wound healing, potentially leading to severe outcomes such as sepsis, underscoring the importance of infection control as a critical challenge in wound management [9].

Traditional treatments, including passive dressings and topical agents, often fail to adequately support healing, particularly in complex chronic wounds [10,11]. Consequently, there is a growing interest in advanced wound therapies that actively promote granulation tissue formation, re-epithelialization, and angiogenesis. Promising strategies include skin substitutes, bioengineered grafts, growth factor therapies, stem cell treatments, and skin bioprinting [12]. Among these, skin substitutes have become widely adopted in clinical settings [13]; they are typically composed of type I collagen or hyaluronic acid, and may also be seeded with autologous or allogeneic keratinocytes and/or fibroblasts, effectively transforming them into Advanced Therapy Medicinal Products (ATMPs) [14]. These constructs demonstrate excellent biocompatibility, moisture retention, and mechanical strength, while their surface architecture and biochemical composition support cell adhesion, proliferation, and differentiation [13]. In particular, decellularized dermis has emerged as a compelling scaffold for skin regeneration [15]. The dermis, primarily composed of ECM, not only provides structural support but also acts as a reservoir for regenerative signals, e.g., by retaining and concentrating growth factors and other chemical signals in gradients that guide cells, as well as interacting with resident stem cells to maintain a balance between self-renewal and differentiation [16–22]. Several decellularized dermis-based products – derived from human (e.g., AlloDerm® and DermACELL®) or animal sources (e.g., Permacol® and SurgiMend®) – are commercially available. These scaffolds proved biocompatible and immunologically inert due to the removal of cellular components, and they provide an ECM architecture that supports cell infiltration and vascularization. Additionally, decellularization reduces the pathogen load, thereby lowering the risk of infection. However, in some cases, the scaffold may exhibit delayed integration into the host tissue, potentially slowing the overall healing process [23].

To address this limitation, coupling decellularized dermis with mesenchymal stromal cells (MSCs) has been proposed, particularly in scenarios where cell proliferation and differentiation are impaired, inflammation remains unresolved, and angiogenesis is insufficient [24–28]. However, its transformation into an ATMP affects its regulatory classification (it is no longer considered a medical device) and its shelf life and storage logistics, thereby representing a limitation. Properly, recent research has shown that the MSC-secretome – comprising freely soluble growth factors and extracellular vesicles (EVs) – is the primary driver of MSC-mediated repair, including wound healing [29,30]. In this context, our prior work demonstrated that a freeze-dried formulation of this secretome – the lyosecretome, obtained through a Good Manufacturing Practice (GMP)-compliant production process – enhances fibroblast migration, granulation tissue formation, neovascularization, and collagen deposition when tested in a murine wound model [31], in accordance with the literature [32–37]. Proteomic analyses confirmed that lyosecretome upregulates key wound-healing proteins, including Fga, Fgg, F13a1, Tnc, Arg1, Anxa5, Col1a1, Dcn, Egfr, and nucleolin, a marker of angiogenesis [31,38–40]. Moreover, according to recent literature, there is also the possibility of "educating" MSCs by manipulating the cell culture microenvironment, thereby tailoring the secretome's biological composition and activity for therapeutic purposes, such as wound healing [41].

Based on this rationale, the current study aimed to develop and evaluate a wound-healing construct by integrating decellularized dermis with MSC-derived lyosecretome. At first, the decellularization protocols were optimized to ensure efficient cell removal while preserving ECM integrity. The resulting scaffolds were then freeze-dried and characterized by Fourier transform infrared (FTIR) spectroscopy, thermogravimetric analysis (TGA), confocal and scanning electron microscopy (SEM), and cytocompatibility testing after seeding human dermal fibroblasts. MSCs were cultured under serum-starved conditions with or without IL-1β or hypoxic stimulation, and the secretome was harvested and processed into lyosecretome via ultrafiltration and lyophilization. Lyosecretomes were then passively loaded onto decellularized dermal scaffolds, and their bioactivity was assessed using in vitro scratch assays on human dermal fibroblasts and human umbilical vein endothelial cells (HUVEC). Of note, high-throughput proteomic analysis characterized signatures in secretomes across MSC-stimulating conditions, shedding light on several factors involved in wound repair.

Table 1
Concentrations of the reagents used in the decellularization protocols.

Protocol	Concentration (M)						
	SDS	TRIS-HCl	EDTA	CHAPS	NaCl	KCl	HEPES
1.5TE	-	0.075	0.0075	0.024	0.165	-	-
2TE	-	0.100	0.0100	0.033	0.220	-	-
1.5K	-	-	-	0.024	-	2.250	0.750
2K	-	-	-	0.033	-	3.000	1.000
CS	-	0.050	0.0050	0.016	0.110	-	-
	0.0035	0.005	0.0005	-	0.015	-	-

2. Materials and methods

2.1. Materials and reagents

Cell culture media, phosphate-buffered saline (PBS), Fetal Bovine Serum (FBS) and antibiotics were purchased from Euroclone, Milan, Italy. 3-((3-Cholamidopropyl)Dimethylammonio)-1-Propanesulfonate (CHAPS), 3-(4,5-dimethylthiazol-2-yl)-2,5-diphenyltetrazolium bromide (MTT), 4-(2-hydroxyethyl)-1-piperazineethanesulfonic acid (HEPES), acetone, acetonitrile, Alexafluor 633 phalloidin, bovine serum albumin (BSA), dimethyl sulfoxide, ethylenediaminetetraacetic acid (EDTA), formalin/formaldehyde, formic acid, Hoechst 33342 (DAPI), IL-1β, mannitol, Nile red, phosphatidylcholine (PC), potassium chloride (KCl), sodium chloride (NaCl), sodium dodecyl sulfate (SDS), trifluoroacetic acid (TFA), tris-(hydroxymethyl)aminomethane-hydrochloride (TRIS) were purchased from Sigma Aldrich, Milan, Italy. All reagents were of analytical grade. Sequencing Grade Modified Trypsin was purchased from Promega Inc., Madison, WI, USA, and RapiGest SF was obtained from Waters Corporation, Milford, MA, USA. HUVEC, HeLa and human fibroblasts were purchased from Promocell, Heidelberg, Germany.

2.2. Preparation of the freeze-dried dermis scaffolds

2.2.1. Collection of dermis samples

The human skin was collected by the Azienda Socio Sanitaria Territoriale (ASST) Grande Ospedale Metropolitano Niguarda's surgical team, according to the standard guidelines applied for skin collection from cadaver donors, and then processed under a Class II B laminar flow hood in a Grade C (GMP) environment at the Tissue Bank, ASST Grande Ospedale Metropolitano Niguarda, Milan. All the experimental procedures were conducted in accordance with the ethical guidelines and regulations set by the relevant institutional review board. Briefly, the grafts were obtained from the lower back and upper thighs of 8 donors (18-70 years old), with informed consent, using a dermatome (Zimmer) with a set thickness of 0.8-1 mm. After being collected, the graft was stored in PBS solution at 4 °C for a maximum of 48 h, then processed and refined to obtain linear margins, measured, and finally transferred into aluminum pouches (of various sizes based on the size of the graft) containing 10 mL of dimethyl sulfoxide as a cryoprotectant for long-term storage at −80 °C.

2.2.2. Dermis decellularization

After thawing, the dermis graft was washed in PBS to remove any remaining cryoprotectant, cut into pieces measuring $2 \times 2\ cm^2$ each, and then decellularized using CHAPS and SDS as surfactants [42]. The concentration of the two surfactants in the protocols was optimized, as reported in Table 1.

Each tissue fragment was incubated with 10 mL of surfactant solution (pH 8) at 37 °C for 16 h under constant agitation on a rocking plate set at 300 rpm. For the CS protocol, the grafts were sequentially treated with the two distinct solutions for 8 h each under the same conditions (37 °C, 300 rpm). Between treatments, the samples were stored overnight at 4 °C in PBS before being transferred to the second solution the following day. The decellularization was repeated three times for each dermis sample; then, the samples underwent a series of washes: 20 min in a hypotonic solution (pH 8) containing 10 mM TRIS, 0.1% NaCl, and 1 mM EDTA, followed by 40 min in PBS, 40 min in sterile injectable water, 20 min in PBS, and a final 20 min rinse in sterile injectable water.

The effective decellularization of the samples was assessed by staining the cell nuclei with DAPI before analysis using confocal microscopy, as further detailed in Section 2.3.2, and by quantifying DNA. To this end, DNA was extracted using the CSC DNA FFPE Kit AS1350 (Promega Inc., Madison, WI, USA) and the Maxwell CSC AS6000 platform. Quantification was performed with a Tecan Infinite 200 Pro.

2.2.3. Dermis freeze-drying

Decellularized dermis samples were freeze-dried using a Martin Christ LSC Plus (Christ GmbH, Osterode am Harz, Germany) located under a laminar flow hood within a Class C section, in accordance with GMP standards. The lyophilization protocol was developed based on the literature [43], with some adjustments. After being transferred without lyoprotectant into vials and placed on metallic shelves, the samples were frozen and held at −40 °C for 90 min. The initial shelf temperature during the primary drying process was set to −35 °C and 0.07 mbar for 180 min. Under a pressure of 0.22 mbar, the samples were heated and held for 60 min at each of the following temperatures: −30 °C, −20 °C, 0 °C, 5 °C, and 10 °C. The primary drying process was concluded by leaving the samples overnight at 15 °C under 0.07 mbar. In the secondary drying process, the shelf temperature was maintained at 25 °C for 180 min.

At the end of the process, the freeze-dried dermis scaffolds were collected from the support and stored at room temperature in vacuum-sealed plastic bags.

2.3. Characterization of the freeze-dried dermis scaffolds

2.3.1. Scanning electron microscopy (SEM)

The scaffold's surface and morphology were observed by SEM (Zeiss, EVO 50 EP model) operating at 15 kV. Before the analysis, the samples were sputter-coated with a thin layer of gold (Edward Sputter Coater 5150B).

2.3.2. Multiphoton confocal microscopy

Fibrillar collagen within the dermal scaffolds was visualized using second harmonic generation (SHG) imaging performed on a multiphoton confocal microscope. Samples were stained with DAPI according to the manufacturer's instructions and mounted on glass-bottom dishes and maintained in PBS during imaging to preserve their native structure and integrity. Imaging was conducted using a Leica STELLARIS DIVE multiphoton microscope equipped with a femtosecond-pulsed Ti:Sapphire Mai Tai HP laser (tuned to 800 nm). SHG signals were collected through HC FLUOTAR L 25x/0.95 W VISIR objective in the backward (epi-) direction using a non-descanned detector and a bandpass filter centered at 400 nm (±20 nm), which corresponds to the second harmonic of the excitation wavelength. Fibrillar collagen was visualized as a white signal in the SHG channel, distinguishing it from background autofluorescence or other tissue components.

2.3.3. Fourier-transform infrared spectroscopy (FTIR)

A Bruker ALPHA II spectrometer (Bruker, Ettlingen, Germany) equipped with a monolithic diamond crystal ATR (Attenuated Total Reflection) accessory and DTGS (deuterated triglycine sulfate) pyroelectric detector was used to record ATR-FTIR spectra of decellularized and non-decellularized freeze-dried dermis scaffolds (10 μm in thickness) in the 400-4000 cm^{-1} range at a 4 cm^{-1} resolution. OPUS software (Release 8.7) was used for processing ATR-FTIR spectra.

2.3.4. Thermo-gravimetric analysis (TGA)

Thermo-gravimetric analysis (TGA) was conducted to investigate the thermal stability and degradation behaviour of the decellularized and non-decellularized freeze-dried dermis scaffolds. Precisely weighed amounts of each sample were analyzed over a temperature range of 25-600 °C at a heating rate of 10 °C/min, with a N_2 stream of 20 mL/min, using a TGA 4000 (PerkinElmer, Milan, Italy).

2.3.5. Swelling test

The ability of decellularized and non-decellularized freeze-dried dermis scaffolds to absorb exudates was evaluated by monitoring the progressive weight gain of the samples (average mass = 0.029 ± 0.014 g, n = 18) put in contact with PBS at different time points. Before weighing, the excess PBS was removed by blotting the dermis scaffold on filter paper. The swelling % (S) was calculated using the following equation:

$$S = \frac{W_t}{W_0} \times 100$$

where W_t is the weight of the scaffold at the time point t, and W_0 is the weight of the same scaffold at the dry state.

2.3.6. In vitro biological studies

Human dermal fibroblasts at P1 were seeded on decellularized and non-decellularized freeze-dried dermis scaffolds. Briefly, each scaffold was reduced with surgical scissors to $0.5 \times 0.5\ cm^2$ and placed at the bottom of a well in a 96-well plate that was not suitable for cell adhesion. Then, cells suspended in a 10 μL drop (5000 cells) were placed on each sample and allowed to absorb for 30 min while incubated at 37 °C, 5% CO_2, before 200 μL of complete medium (DMEM High Glucose, 10% FBS, 1% glutamine, 0.5% penicillin-streptomycin, 0.5% amphotericin B) were added, ensuring that the dermis samples were submerged entirely. Samples were cultured for up to 15 days, with medium changed every 3-4 days. After 1, 7, and 15 days, an MTT test was performed as already reported [44], and the absorbance of samples at 650 nm was monitored over time.

To further assess cellular growth on decellularized and non-decellularized dermis scaffolds, a histological analysis using Hematoxylin and Eosin (H&E) staining was performed. Briefly, after cell culture, each dermis sample was transferred to a vial containing 1 mL of 10% formalin (4% formaldehyde) for 48 h, then processed routinely to obtain 4 μm sections before staining with H&E. Samples were then observed under an optical microscope (Carl Zeiss 37081).

Finally, the cell morphology of fibroblasts cultured for 15 days on decellularized and non-decellularized dermis scaffolds was assessed using a laser-scanning confocal microscope (Andor BC43, Oxford Instruments). After being fixed in 3.7% formaldehyde for 15 min at 37 °C, the samples were washed with PBS and incubated for 45 min in PBS containing 1% BSA and 10% FBS before being stained with Alexafluor 633 phalloidin and DAPI to stain the cytoskeleton and nuclei, respectively, according to the manufacturer's instructions. The acquired images were processed and analyzed using the image analysis software Imaris Viewer, Oxford Instruments.

2.4. Preparation and characterization of MSC-lyosecretome-loaded dermis scaffolds

2.4.1. MSC-lyosecretome preparation and characterization

MSC-lyosecretome was prepared and characterized according to previously reported procedures that are compliant with GMP [45,46]. Briefly, adipose-derived MSCs were seeded into flasks (10,000 cells/cm^2) at 37 °C and 5% CO_2 and expanded in DMEM/F12 minimal medium plus 10% v/v FBS, 1% v/v penicillin/streptomycin, and 1% v/v amphotericin B until P3. MSCs used met the requirements needed for clinical use in terms of identity (as stated by the International Society for Cellular Therapy [47]) and sterility (according to Eu. Ph. 11.0, 2.6.27).

The release of secretome was induced by culturing MSCs in DMEM/F12 without FBS (serum starvation), either alone or in combination with IL-1β or hypoxia (5% O_2). In detail, for the pro-inflammatory condition, cells were pre-treated with IL-1β (10 ng/mL) for 48 h before serum starvation. For the hypoxic condition, cells were cultured under 5% O_2 while undergoing serum starvation simultaneously. The cell culture supernatants were collected after 48 h, centrifuged at 3500× *g* for 10 min, and then ultrafiltered by tangential flow filtration (KrosFlo® Research 2i system, Spectrum Laboratories, Milan, Italy) using a filtration module with a superficial area of 235 cm^2 and a molecular weight cut-off of 5 kDa (Spectrum Laboratories, Milan, Italy). During the process, the samples were first concentrated to a protein concentration of 115 μg/mL [46] and then diafiltered using sterile ultrapure water as the buffer. Once concentrated and purified, mannitol (0.5% w/v) was added to the secretome, which was then frozen at −80 °C and freeze-dried (Christ Epsilon 2-16D LSCplus) at 8×10^{-1} mbar and −50 °C for 72 h. The obtained lyosecretome was stored at −20 °C until use (within 12 months).

Lyosecretome was fully characterized for total protein and lipid content using a BCA Protein Assay Kit (Thermo Fisher Scientific, Milan, Italy) and a Nile red assay, as well as particle size distribution by nanoparticle tracking analysis (NTA), as previously reported [45,46].

2.4.2. MSC-lyosecretome loading into dermis scaffolds

Each dermis sample (approximately 40 mg) was loaded with lyosecretome to achieve a protein-to-dermis ratio of 50 μg protein per mg dermis. Briefly, lyosecretome was solubilized in deionized water, and a drop of the solution (volume ranging from 40 to 100 μL to achieve the appropriate protein loading reported above) was placed on each dermis scaffold and allowed to absorb for 10 min at room temperature. Samples were then frozen at −80 °C and freeze-dried (Christ Epsilon 2-16D LSCplus) at 8×10^{-1} mbar and −50 °C for 24 h.

2.4.3. In vitro secretome release test

Dermis scaffolds loaded with lyosecretome (from serum-starved MSCs) were immersed in 5 mL of PBS pH 7.2 at room temperature. At fixed time intervals, 500 μL of the release medium was collected to assess the proteins and lipids released [48,49], and was then replaced with an equivalent amount of fresh PBS. All analyses were conducted in triplicate, and the cumulative percentage of released proteins and lipids was calculated using the following equation:

$$\textit{Cumulative amount of drug released}\ (\%) = \frac{C_i}{C_0} \times 100$$

where C_i is the amount of the proteins/lipids released at a definite time interval, and C_0 is the loaded protein/lipid amount (it is assumed that the encapsulation efficiency is 100%, as the drop of the lyosecretome solution was adsorbed entirely and fully retained by dermis scaffolds).

2.4.4. Drug release kinetic study

The mechanism and kinetics of drug release were characterized by fitting in vitro drug release data to various kinetic models.

Higuchi

$$F(t) = k \times t^{0.5}$$

$$F(t) = 100 \times (1\text{-}C \times \exp^{(-k \times t)})$$

where F(t) is the amount of drug released at time t, and *k* is the release constant. The latter equation is equation (2.12) from Ref. [50].

Peppas-Sahlin

$$F(t) = k_1 \times t^m + k_2 \times t^{(2 \times m)}$$

where F(t) is the amount of drug released at time t, k_1 and k_2 are, respectively, the diffusion and erosion constants, and *m* is the diffusional exponent indicative of the drug release mechanism.

Ritger-Peppas

$$F(t) = k \times t^n$$

where F(t) is the amount of drug released at time t, *k* is the release constant, and *n* is the release exponent, indicative of the drug release mechanism.

Zero-order

$$F(t) = k \times t$$

where F(t) is the amount of drug released at time t, and *k* is the release constant.

Korsmeyer-Peppas

$$F(t) = k_{KP} \times t^n \times Q_0$$

where F(t) is the amount of drug released at time t, k_{KP} is the release constant, *n* is the release exponent indicative of the drug release mechanism, and Q_0 is the initial amount of drug.

2.5. In vitro healing test

2.5.1. Generation of stable GFP-expressing human fibroblasts and HUVECs

Lentiviral particles were generated using an ultracentrifugation protocol as described elsewhere [51]. Briefly, fibroblasts or HUVECs were plated in 10 cm Petri dishes at a density of 1×10^6 per dish; after 16 h, cells were transfected with plasmids of a third-generation lentiviral system (1.4 μg pMDLg.pRRE, 0.5 μg pRSV.Rev, 0.75 μg pMD2.VSVG, and 4 μg of pRRLSIN.cPPT.PGK-GFP.WPRE). Transfection was performed using Lipofectamine 2000 (10 μL per dish) according to the manufacturer's instructions (Invitrogen, Milan, Italy) in a final volume of 7 mL/dish of complete medium (DMEM, 10% FBS, 1% Pen/Strep, and 2 mM glutamine for fibroblasts and EndoGRO-MV-VEGF Complete Culture Media for the HUVEC). 48-72 h after transfection, lentiviral particles were collected by ultracentrifugation (50,000× *g*, 2 h) using a high-speed ultracentrifuge (Himac CR30NX, Eppendorf) and a swinging bucket rotor (R25ST). The supernatants were discarded, and the pellet was resuspended in 200 μL of culture medium. The viral titer was determined by infecting HeLa cells (1×10^4 cells in a 24-well plate) with serial dilutions of the viral stock [51]. A multiplicity of infection (MOI) of 3-4 was used for transduction of target cells. Target cells were plated in 35 mm Petri dishes (1×10^5 cells) and transduced with an MOI of 3-4 in a total volume of 1 mL of complete medium. 24 h after transduction, 2 mL of complete medium were added. Routinely, 100% of transduction was achieved. After three passages, cells were cryopreserved and used for experiments.

2.5.2. Wound healing assay

GFP-expressing fibroblasts or HUVECs were seeded at a density of 40,000 cells/cm^2 in a 24-well plate and then scraped with a sterile pipette tip to create a linear "scratch". Dermis scaffolds, loaded with lyosecretomes (see section 2.4.2), were placed above the scratch, and samples were incubated at 37 °C and 5% CO_2 for 48 h. Images were acquired using a Leica THUNDER Imager 3D Live Cell with a peak

fluorescence emission of 509 nm, taken every 2 h.

A custom Matlab®-based script was developed and optimized to quantify wound healing in scratch assays. The workflow was initiated by manually selecting the wound area at time zero (t_0), generating a binary mask over a reference image that served as a reference for all subsequent images. These images were analyzed using the same mask parameters in batch processing. Once the initial mask was defined, the script automatically processes subsequent images acquired at different time points in .tif format (2048 × 2048 pixels). For each image, the green channel is extracted, then a median filter is applied to remove salt-and-pepper noise. A Fast Fourier Transform bandpass smooth filter is then applied to enhance the contrast of objects while simultaneously reducing background noise, with foreground structures considered within the 3-40 pixel range. The filtered images were converted into binary masks by stretching the histogram around the main intensity peak and performing Otsu thresholding. Image segmentation was performed using morphological dilation with a disk-shaped structuring element of radius 10, and objects smaller than 3000 pixels were removed to isolate the wound area. The wound area considered for analysis was defined as the sum of the three largest identified regions. The algorithm calculates the wound area (in pixels) at each time point, which was then normalized to the initial area at t_0 to determine the percentage of wound closure over time. The workflow included a setup step to define input parameters and the file structure, and a batch-processing step that analyzed the entire time series. By standardizing image-processing parameters and minimizing manual intervention, this semi-automated method ensured reproducible, operator-independent quantification of wound-healing dynamics. The results obtained with the Matlab® script were compared with those from the ImageJ workflow as described in the Supplementary file F1. Raw scratch assay images and the custom Matlab® script used for this analysis are publicly available, as part of a broader Figshare collection (see Data Availability Statement).

2.6. Proteomic characterization of lyosecretome

2.6.1. Sample preparation for proteomic analysis

Proteomic analysis was performed on 3 biological replicates per condition. 1 mL of each MSC-secretome sample, collected after ultrafiltration and before the addition of cryoprotectant, was concentrated to 50 µL using a vacuum concentrator (Savant Instruments, Farmingdale, NY, USA). Protein denaturation was achieved by adding RapiGest SF to a final concentration of 0.25% w/v, followed by incubation at 95 °C for 20 min. Samples were then cooled to room temperature and centrifuged at 2200× *g* for 10 min. Subsequently, 50 ± 0.5 µg of protein from each sample was enzymatically digested using Sequencing Grade Modified Trypsin at an enzyme-to-substrate ratio of 1:50 w/w and incubated overnight at 37 °C. The next day, a second aliquot of trypsin was added at a 1:100 w/w ratio, and digestion was continued for an additional 4 h. The digestion reaction was stopped by acidification with 0.5% TFA, followed by incubation at 37 °C for 45 min. To remove degradation products of RapiGest SF, the sample was centrifuged at 13000× *g* for 10 min. Peptides were desalted using C-18 spin columns (G-Biosciences, St. Louis, MO, USA), according to the manufacturer's protocol, and then concentrated using a vacuum concentrator at 60 °C. Finally, the sample was resuspended in 0.1% formic acid to achieve a final peptide concentration of 0.1 µg/µL.

2.6.2. LC-MS/MS analysis

Trypsin-digested samples were analyzed using Eksigent nanoLC-Ultra® 2D System (Eksigent, part of AB SCIEX Dublin, CA, USA), configured in trap-elute mode. For each analysis, 0.8 µg of digested peptides were first loaded onto a trap (10 mm × 75 µm, nano trap RP-1 C18-CL, 3 µm, 120 Å, Phenomenex, Torrance, CA, USA) and run with 0.1% formic acid at a flow rate of 3 µL/min for 10 min, maintained at a temperature of 35 °C. Peptides were then eluted onto a nano reversed phase column (75 µm × 25 cm bioZen Peptide XB-C18, 2.6 µm, 120 Å, Phenomenex) through a 105-min gradient of eluent B (eluent A, 0.1% formic acid in water; eluent B, 0.1% formic acid in acetonitrile) at a flow rate of 300 nL/min. In detail, the gradient was as follows: from 3 to 8% B in 2 min, 8-30% B in 58 min, 30-40% B in 10 min, 40-80% B in 2 min, and holding at 80% B for 6 min. Then, the column was re-equilibrated from 97% to 3% B in 2 min and stayed for 25 min at 3% B. Mass spectra were acquired using a TripleTOF® 6600+ mass spectrometer (AB Sciex Pte. Ltd. Marsiling Ind Estate Road 3, Woodlands Central Indus. Estate, Singapore) equipped with OptiFlow® Turbo V source using SteadySpray™ nano probe and 20 µm electrodes, operating at 3 kV, for peptide ionization. Full mass spectra were recorded in positive ion mode over the 400-1250 *m/z* range, with a resolution of 60,000 FWHM (at *m/z* 200). Each full scan was followed by dependent MS/MS scans, acquired at 15,000 FWHM resolution, with a mass range of 200-1250 *m/z* (50 ms accumulation time). A maximum of 30 candidate ions, exceeding the threshold of 200 cps, were selected using an isolation width of 0.7 *m/z* on a Q1 and an accumulation time of 250 ms with a dynamic exclusion of 15 s. Precursor peptides were further fragmented by collision-induced dissociation, using N_2 as an inert gas to generate MS/MS spectra in high-sensitivity mode, each with a 50-ms accumulation time. Charge states from 2+ to 4+ were chosen for ion selection. A rolling collision energy with a collision energy spread of 5 eV was used. Mass spectrometer scan functions and high-performance liquid chromatography solvent gradients were controlled by the Analyst software version 1.8.1 (SCIEX) and Eksigent Control Software version 4.3 (Eksigent, part of AB SCIEX, Dublin, CA, USA), respectively.

2.6.3. MS/MS data processing

TripleTOF data (wiff and wiffscan files) were converted into an mzML file with MSConvert, part of the ProteoWizard software suite [52]. Data analysis was performed using Proteome Discoverer version 2.5, which employed the SEQUEST HT search algorithm [53]. The experimental MS/MS spectra were matched against the *in silico* tryptic peptide sequences of the *Homo sapiens* protein database (105,089 sequences) obtained from the UNIPROT repository in October 2024. Identification parameters included a precursor ion mass tolerance of 20 ppm and a fragment ion tolerance of 0.1 Da. Up to 3 missed cleavages per peptide were allowed. A percolator node was used with a target-decoy strategy to give a final false discovery rate (FDR) ≤ 0.01 (strict) based on q-values, considering a maximum ΔCN of 0.05. Identification thresholds required a minimum cross-correlation of 1. Only proteins with rank 1 and peptides with medium confidence were retained. A FDR ≤1% was enforced for all identifications.

To provide a rank list of the most abundant proteins in the analyzed samples, the average Peptide Spectrum Matches (PSMs) of each protein was normalized based on the following formula:

$$nPSM = \frac{PSM}{MW} \times 110$$

where MW represents the molecular weight of a given protein, and 110 is the average molecular weight of an amino acid.

Venn diagram and constrained Principal Coordinate Analysis (cPCoA) were performed by ImageGP 2 (available at https://www.bic.ac.cn/BIC). The Functional Annotation Tool of the STRING database was used to characterize the most enriched GO terms for molecular function, biological processes, and cellular component across all conditions (serum starvation, IL-1β, hypoxia). Terms uniquely enriched in each secretome were identified through pairwise comparison and selected by Dave Index [54]; the top 10 best-ranked terms are reported based on the STRING signal score [55].

A protein-protein interaction (PPI) network was built by combining wound healing-related proteins and the *Homo sapiens* PPI network reconstructed through Cytoscape's STRING APP [56]; only experiment (score >0.15) and database (score >0.30) annotated PPIs were considered.

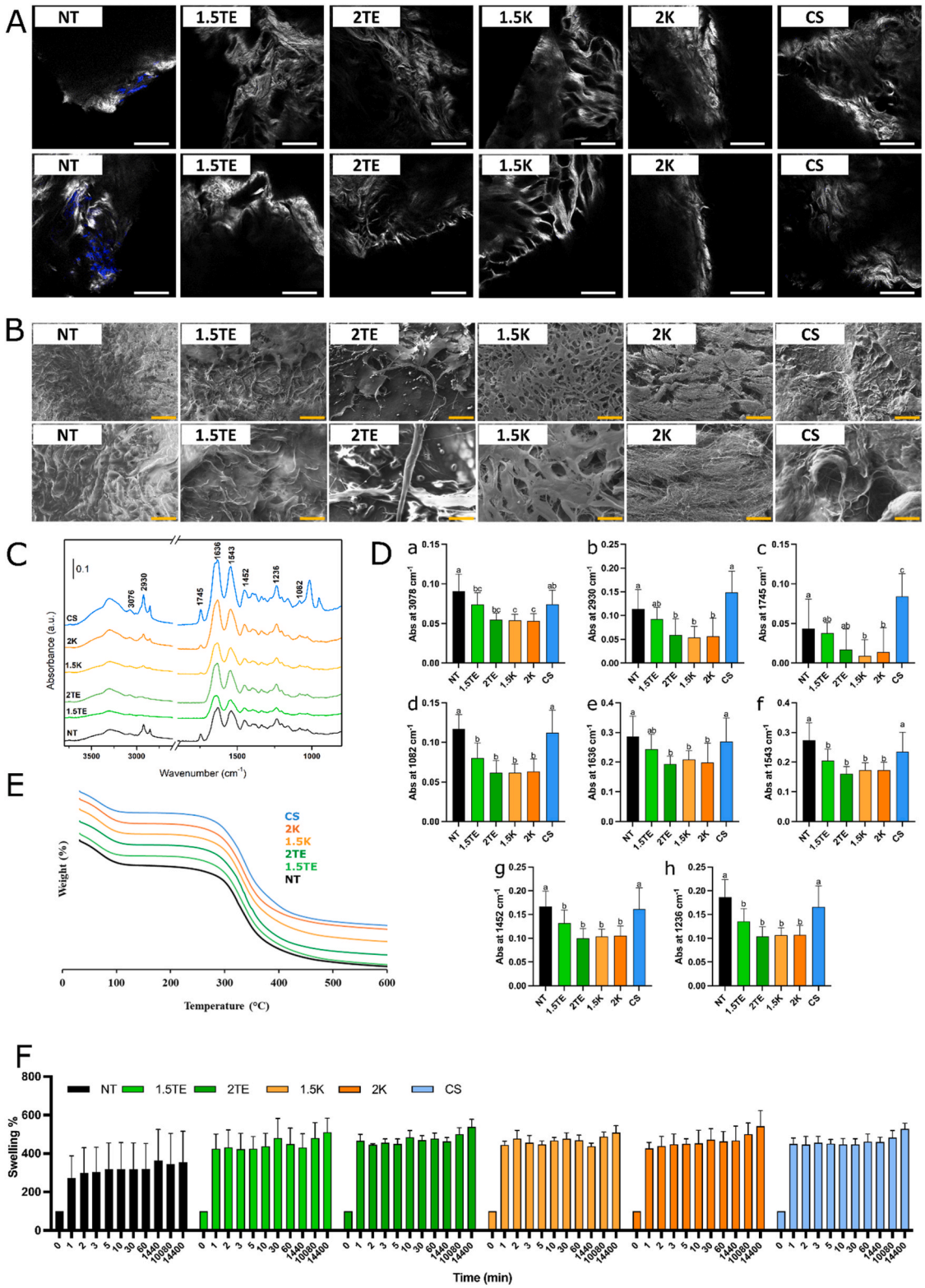

Fig. 1. (**A**) Multiphoton confocal images of freeze-dried dermis samples, either non-decellularized (NT) or decellularized using the 1.5TE, 2TE, 1.5K, 2K, and CS protocols; scale bar: 100 μm. Cell nuclei are stained blue, while fibrillar collagen is visualized in white via SHG imaging. (**B**) SEM images of NT freeze-dried dermis samples and those decellularized using the 1.5TE, 2TE, 1.5K, 2K, and CS protocols. Images were captured at 500× (upper row) and 1.5k× (lower row) magnifications; scale bar: 100 μm. (**C**) FTIR spectra of decellularized and NT dermis scaffolds in the mid-infrared region (4000-400 cm^{-1}). (**D**) Absorbance intensities corresponding to lipid (a-d) and collagen (e-h) components. Different letters (a, ab, b, bc, c) indicate statistically significant differences between groups ($p < 0.05$); identical letters indicate no significant difference ($p > 0.05$). Data are reported as mean ± standard deviation. Statistical analysis was performed using one-way ANOVA followed by Tukey's multiple comparison test ($n = 13$ per condition). (**E**) Thermogravimetric (stacked) profiles of freeze-dried dermis samples, either NT or decellularized using the 1.5TE, 2TE, 1.5K, 2K, and CS protocols. (**F**) PBS uptake capacity of freeze-dried dermis scaffolds, expressed as weight gain (g/g) relative to dry weight over time. Results are reported as mean ± standard deviation ($n = 3$). (For interpretation of the references to color in this figure legend, the reader is referred to the Web version of this article.)

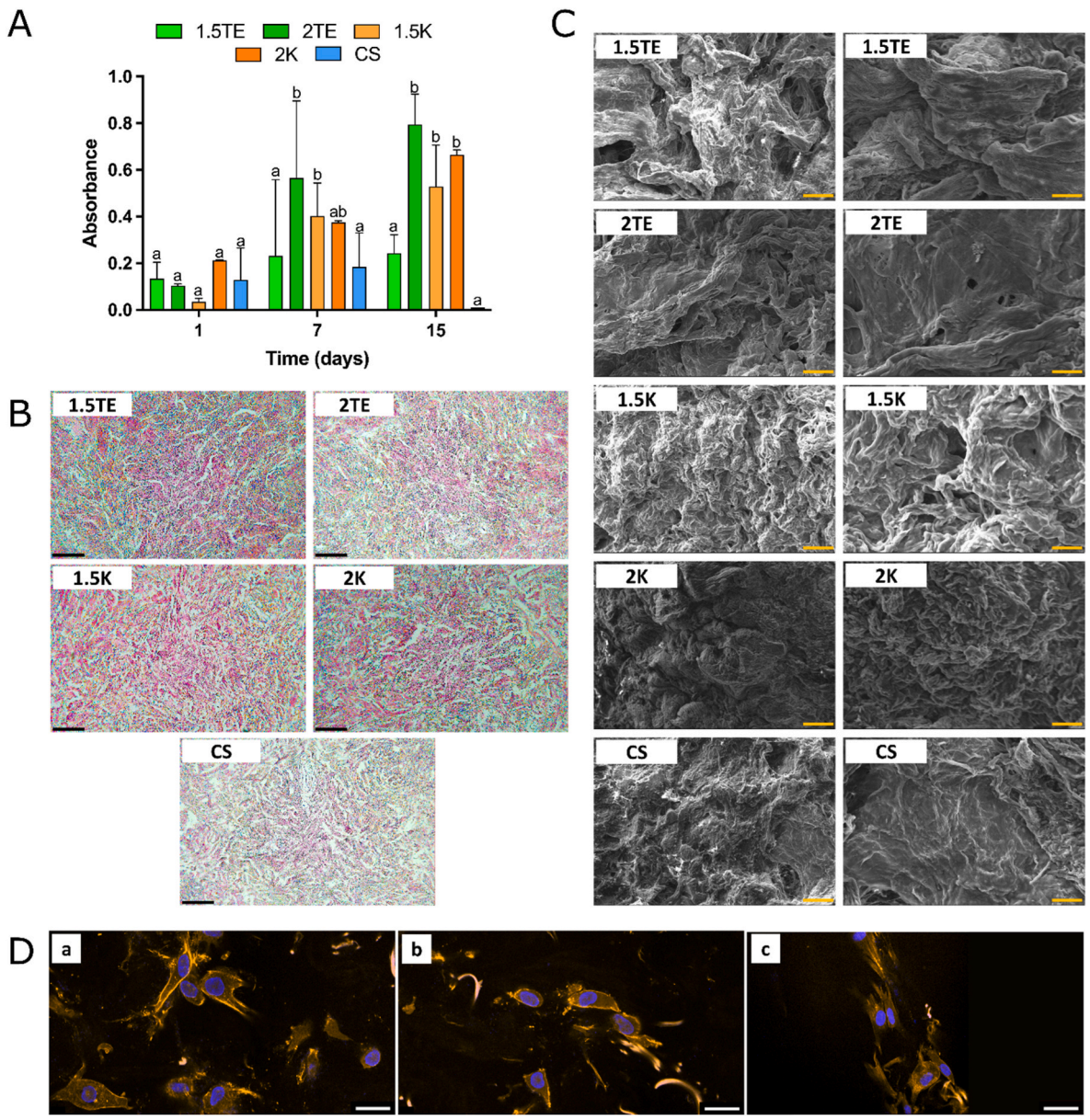

Fig. 2. (**A**) Viability of fibroblasts cultured on freeze-dried decellularized dermis scaffolds, assessed by MTT assay and expressed as the mean absorbance at 650 nm. Different letters (a, ab, b) indicate statistically significant differences between groups ($p < 0.05$); identical letters indicate no significant difference ($p > 0.05$). Data are presented as mean ± standard deviation; statistical analysis was performed using two-way ANOVA followed by Fisher's LSD test ($n = 2$). (**B**) H&E staining of freeze-dried dermis scaffolds seeded with fibroblasts and cultured for 15 days; magnification: 12.5×, scale bar: 200 μm. (**C**) SEM images of freeze-dried dermis scaffolds seeded with fibroblasts and cultured for 15 days; 500× (left column) and 1.5k× (right column) magnifications, scale bar: 20 μm. (**D**) Representative confocal images of fibroblasts cultured on freeze-dried dermis scaffolds after 15 days shown for 1.5TE, 1.5K and 2K decellularization protocols representative of the five conditions tested; scale bar: 20 μm. Cell nuclei are stained in blue; the cytoskeleton is stained in orange. Confocal imaging was acquired on a representative subset of conditions; morphological evaluation across all five protocols is supported by the SEM and H&E analyses shown in panels B and C. (For interpretation of the references to color in this figure legend, the reader is referred to the Web version of this article.)

2.7. Statistical analysis

Raw data were processed using Statgraphics XVII (Statpoint Technologies, Inc., Warrenton, VA, USA) or GraphPad Prism (version 8.02, GraphPad Software, Boston, MA, USA). A linear generalized analysis of variance (ANOVA) model was applied to analyze the data with a normal distribution, and the differences between the groups were evaluated using Tukey's or least significant difference (LSD) procedure, as detailed in the caption of the figures. The statistical significance was set at $p < 0.05$.

3. Results

3.1. Evaluation of decellularization efficiency and its impact on dermal scaffold properties

Dermis samples were decellularized using five different protocols and subsequently freeze-dried to ensure long-term stability and readiness for application. The efficiency of decellularization and its impact on scaffold microstructure and lipid and collagen content were thoroughly evaluated.

Successful removal of cellular material was confirmed by DNA quantification, which consistently showed values below 50 ng/mg

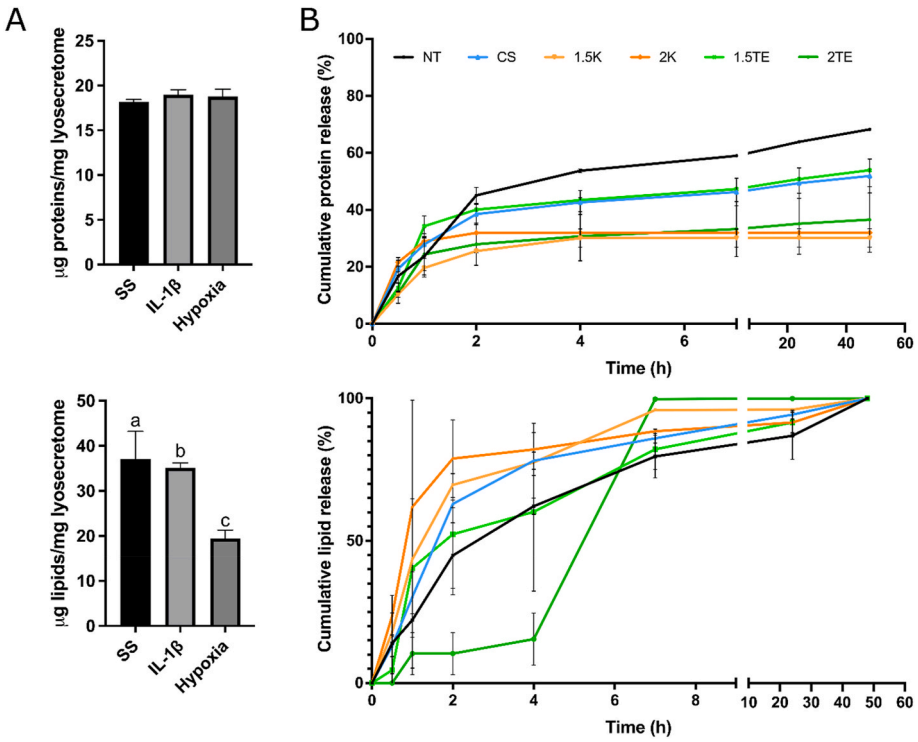

Fig. 3. (**A**) Protein and lipid content of lyosecretomes produced from MSCs by serum starvation (SS), with or without stimulation with IL-1β or hypoxia (5% O_2). Data are presented as mean ± standard deviation. Statistical analysis was performed using one-way ANOVA followed by Tukey's multiple comparison test (n = 3). Different letters (a, b, c) indicate statistically significant differences between groups ($p < 0.05$). (**B**) In vitro protein and lipid release profiles from freeze-dried dermis scaffolds immersed in pH 7.2 PBS at room temperature. Data are presented as mean values ± least significant difference (LSD); Multifactor ANOVA and Fisher's LSD test for multiple comparisons, n = 3. The overlap of two LSD intervals graphically indicates the absence of a significant difference ($p > 0.05$).

(Table S1), and further validated by the absence of cell nuclei under multiphoton confocal microscopy with SHG imaging (Fig. 1A). In the untreated dermis (NT), collagen fibers appeared interwoven with nuclei (stained in blue), reflecting the presence of native cells within the ECM. Following treatment, the structural features varied depending on the protocol: the 1.5TE and 2TE methods produced dense, continuous collagen bundles with minimal disturbance of native organization, whereas the 1.5K treatment generated a more porous scaffold characterized by regularly aligned fibers and enhanced pore uniformity. By contrast, the 2K protocol maintained a compact, stratified collagen arrangement with fewer open spaces, whereas the CS sample exhibited a highly organized, interconnected fibrillar morphology. SEM analysis supported these observations (Fig. 1B). NT samples displayed a dense, compact structure rich in cells and residual material. After decellularization, distinct morphological changes emerged: 1.5TE samples showed greater collagen exposure but retained irregularities; the 2TE protocol was more aggressive, exposing the underlying matrix while introducing localized disruption. In contrast, the 1.5K treatment produced a more porous and uniform scaffold, with clearly distinguishable fibers and evenly distributed pores, whereas the 2K protocol yielded a compact, stratified lamellar arrangement. Finally, the CS method generated a well-organized fibrillar network resembling the morphology of native collagen. Collectively, these results indicate that all protocols preserved the overall collagen network; however, the 1.5K method most effectively enhanced porosity, whereas the TE-based approaches produced denser, more compact matrices.

FTIR spectroscopy was performed to investigate potential compositional differences among the scaffolds. Representative spectra of decellularized and NT freeze-dried dermis samples are shown in Fig. 1C, highlighting characteristic peaks commonly observed in skin-derived biological materials. Lipid components were identified by the peaks related to νC-H at 3078 cm^{-1}, the νC-H stretching in $–CH_3$ and CH_2 at 2855, 2930 and 2954 cm^{-1}, the νC=O in esters at 1745 cm^{-1}, as well as phospholipids' PO^{2-} asymmetric and symmetric stretching vibrations which contributed to the signal at 1237 cm^{-1} and are the main responsible of the peack at 1082 cm^{-1} [57]. Protein components, primarily collagen and elastin, exhibited distinctive peaks of amide I (at about 1621 cm^{-1}, νC=O), amide II (at about 1515 cm^{-1}, δN-H + νC-N), and amide III (at about 1230 cm^{-1}, νC-N + δN-H). Additionally, peaks at 1636, 1543, and 1236 cm^{-1} were associated with the stretches of the amide groups of collagen structures, while those between 1450 and 1200 cm^{-1} corresponded to CH bending of collagen [58]. For quantitative comparison between samples, numerical data from absorbance spectra were used. Due to high variability in composition within the same sample, particularly in regions containing hair bulbs, measurements were conducted in areas devoid of hair bulbs to ensure consistency. Absolute peak intensities corresponding to lipids and collagen signatures were evaluated (Fig. 1D): all decellularization protocols significantly reduced lipid content compared to the non-treated (NT) samples ($p < 0.05$), except the CS protocol, which showed no statistically significant difference in residual lipids relative to NT samples ($p > 0.05$). At the same time, the intensity of collagen-associated peaks was slightly but significantly decreased following decellularization (Fig. 1D, panels e-h; $p < 0.05$), with the CS treatment showing no significant deviation from the NT group.

TGA was employed to assess the residual water content and thermal stability of both decellularized and non-decellularized freeze-dried dermis samples. The resulting thermograms (Fig. 1E) revealed a consistent thermal behavior across all samples, regardless of treatment. Two distinct weight-loss phases were observed: the first, occurring below 125 °C and accounting for approximately 12.5%-14.3% of the mass loss, corresponds to the evaporation of bound water associated with collagen and other ECM components, such as elastin and proteoglycans (e.g., hyaluronic acid). The second phase, between 200 and 500 °C, reflects the thermal decomposition of these macromolecules [59, 60]. Thermal properties showed no significant variation between

Table 2
Results of in vitro release model fitting for proteins and lipids from dermis scaffolds. Kinetic elaborations were performed on the cumulative release data obtained from at least three independent experiments for each batch. "~" indicates that the analysis performed was "ambiguous"; therefore, the fit does not nail down the values of all the parameters, and 95% confidence bounds cannot be reported. These latter data were not considered in the interpretation of results.

Model	Equation	Treatment	Proteins/ Lipids	Coefficients (95% Confidence Bounds)	Sum of Squares	R^2	Degrees of Freedom
Higuchi	$F(t) = k \times t^{0.5}$	NT	Proteins	$k = 0.2623$ (0.2002, 0.324)	2.203	0.3615	15
			Lipids	$k = 0.03947$ (0.02774, 0.05120)	0.07858	0.4856	15
		CS	Proteins	$k = 0.1599$ (0.1154, 0.2043)	1.131	−0.01544	15
			Lipids	$k = 0.02386$ (0.01295, 0.03477)	0.068	0.1941	15
		1.5K	Proteins	$k = 0.1146$ (0.07598, 0.1531)	0.8502	−0.1835	15
			Lipids	$k = 0.04219$ (0.02860, 0.05578)	0.1055	0.56	15
		2K	Proteins	$k = 0.1263$ (0.07843, 0.1741)	1.307	−1.179	15
			Lipids	$k = 0.03983$ (0.02676, 0.05289)	0.09753	0.1046	15
		1.5 TE	Proteins	$k = 0.1839$ (0.1320, 0.2357)	1.534	0.03981	15
			Lipids	$k = 0.03566$ (0.02336, 0.04796)	0.07962	0.03809	15
		2 TE	Proteins	$k = 0.1201$ (0.08239, 0.1577)	0.8107	−0.1019	15
			Lipids	$k = 0.01912$ (0.01455, 0.02369)	0.0119	0.711	15
	$F(t) = 100 \times (1 - C \times \exp^{(-k \times t)})$	NT	Proteins	$C = 0.994$ (0.9915, 0.9964) $k = 0.000197$ (7.025×10^{-5}, 0.0003241)	1.922	0.443	14
			Lipids	$C = 0.9993$ (0.9988, 0.9998) $k = 0.00003847$ (1.83×10^{-5}, 6.612×10^{-5})	0.09331	0.3891	14
		CS	Proteins	$C = 0.9958$ (0.9943, 0.9973) $k = 0.00009957$ (2.241×10^{-5}, 0.0001769)	0.7198	0.3538	14
			Lipids	$C = 0.9995$ (0.9990, 0.9999) $k = 0.00001938$ (-4.407×10^{-6}, 4.318×10^{-5})	0.06927	0.179	14
		1.5K	Proteins	$C = 0.9968$ (0.9955, 0.9981) $k = 0.00006107$ (-7.413×10^{-6}, 0.0001297)	0.5696	0.2071	14
			Lipids	$C = 0.9995$ (0.9989, 1.000) $k = 0.00005419$ (2.261×10^{-5}, 8.579×10^{-5})	0.1218	0.4918	14
		2K	Proteins	$C = 0.9958$ (0.9946, 0.9971) $k = 0.00004326$ (-2.250×10^{-5}, 0.0001091)	0.525	0.1244	14
			Lipids	$C = 0.999$ (0.9985, 0.9995) $k = 0.00002653$ (8.433×10^{-7}, 5.223×10^{-5})	0.08065	0.2595	14
		1.5 TE	Proteins	$C = 0.9952$ (0.9935, 0.9970) $k = 0.0001172$ (2.378×10^{-5}, 0.0002108)	1.053	0.341	14
			Lipids	$C = 0.9993$ (0.9988, 0.9999) $k = 0.00003315$ (5.006×10^{-6}, 6.130×10^{-5})	0.08585	0.3325	13
		2 TE	Proteins	$C = 0.9968$ (0.9955, 0.9980) $k = 0.00007045$ (3.887×10^{-6}, 0.0001371)	0.5378	0.2691	14
			Lipids	$C = 0.9998$ (0.9996, 1.000) $k = 0.00002399$ (1.182×10^{-5}, 3.617×10^{-5})	0.01815	0.5607	14
Peppas–Sahlin	$F(t) = k_1 \times t^m + k_2 \times t^{(2 \times m)}$	NT	Proteins	$k_1 = \sim$ $k_2 = \sim$ $m = \sim$	0.282	0.9183	13
			Lipids	$k_1 = \sim$ $k_2 = \sim$ $m = \sim$	0.05656	0.6297	13
		CS	Proteins	$k_1 = \sim$ $k_2 = \sim$ $m = \sim$	0.1264	0.8865	13
			Lipids	$k_1 = \sim$ $k_2 = \sim$ $m = \sim$	0.06235	0.5625	13
		1.5K	Proteins	$k_1 = \sim$ $k_2 = \sim$ $m = \sim$	0.2151	0.7005	13
			Lipids	$k_1 = -0.1611$ (-∞, 0.1167) $k_2 = 0.1304$ (2.630×10^{-7}, 3.225) $m = 0.1997$ (−0.1518, +∞)	0.1041	0.5657	13
		2K	Proteins	$k_1 = \sim$ $k_2 = \sim$ $m = \sim$	0.07451	0.8757	13
			Lipids	$k_1 = \sim$ $k_2 = \sim$ $m = \sim$	0.04192	0.6152	13
		1.5 TE	Proteins	$k_1 = \sim$ $k_2 = \sim$ $m = \sim$	0.2406	0.8494	13
			Lipids	$k_1 = \sim$ $k_2 = \sim$ $m = \sim$	0.06329	0.5079	12
		2 TE	Proteins	$k_1 = \sim$ $k_2 = \sim$ $m = \sim$	0.1879	0.7446	13
			Lipids	$k_1 = 0.01545$ (0.005345, 0.03154) $k_2 = 0.812$ (0.5024, 1.136) $m = -0.0004661$ (-0.002199, -5.037×10^{-5})	0.0007979	0.8068	13

(*continued on next page*)

Table 2 (*continued*)

Model	Equation	Treatment	Proteins/ Lipids	Coefficients (95% Confidence Bounds)	Sum of Squares	R^2	Degrees of Freedom
Ritger–Peppas	$F(t) = k \times t^n$	NT	Proteins	$k = 0.6536$ (0.5267, 0.7848) $n = 0.2094$ (0.1422, 0.2811)	0.4533	0.8686	14
			Lipids	$k = 0.07278$ (0.03213, 0.1202) $n = 0.3083$ (0.1265, 0.5468)	0.06387	0.5818	14
		CS	Proteins	$k = 0.4655$ (0.3880, 0.5448) $n = 0.1558$ (0.09422, 0.2199)	0.1544	0.8614	14
			Lipids	$k = 0.05404$ (0.01501, 0.1009) $n = 0.2416$ (0.0032, 0.6102)	0.05685	0.3263	14
		1.5K	Proteins	$k = 0.3552$ (0.2610, 0.4528) $n = 0.1362$ (0.03556, 0.2426)	0.2347	0.6733	14
			Lipids	$k = 0.04685$ (0.008132, 0.1050) $n = 0.4678$ (0.1971, 0.9455)	0.1052	0.5613	14
		2K	Proteins	$k = 0.49$ (0.4327, 0.5478) $n = 0.05314$ (0.003064, 0.1034)	0.07637	0.8726	14
			Lipids	$k = 0.1089$ (0.06886, 0.1514) $n = 0.1781$ (0.04445, 0.3272)	0.04514	0.5855	14
		1.5 TE	Proteins	$k = 0.5247$ (0.4192, 0.6332) $n = 0.1633$ (0.08978, 0.2408)	0.294	0.816	14
			Lipids	$k = 0.06579$ (0.02265, 0.1178) $n = 0.3079$ (0.08965, 0.6144)	0.06792	0.4719	13
		2 TE	Proteins	$k = 0.3614$ (0.2726, 0.4531) $n = 0.1447$ (0.05238, 0.2425)	0.2046	0.722	14
			Lipids	$k = 0.02244$ (0.008779, 0.04011) $n = 0.4507$ (0.2642, 0.7115)	0.01174	0.7157	14
Zero-order	$F(t) = k \times t$	NT	Proteins	$k = 0.03721$ (0.01977, 0.05466)	5.932	−0.7189	15
			Lipids	$k = 0.005862$ (0.003131, 0.008593)	0.1453	0.04858	15
		CS	Proteins	$k = 0.02219$ (0.01054, 0.03385)	2.646	−1.375	15
			Lipids	$k = 0.003423$ (0.001187, 0.005658)	0.09736	−0.1539	15
		1.5K	Proteins	$k = 0.01551$ (0.006165, 0.02486)	1.701	−1.368	15
			Lipids	$k = 0.006749$ (0.004024, 0.009474)	0.1447	0.3963	15
		2K	Proteins	$k = 0.01658$ (0.005386, 0.02778)	2.442	−3.073	15
			Lipids	$k = 0.005568$ (0.002453, 0.008683)	0.189	−0.7354	15
		1.5 TE	Proteins	$k = 0.02557$ (0.01211, 0.03902)	3.526	−1.207	15
			Lipids	$k = 0.005321$ (0.002603, 0.008038)	0.1326	−0.03087	14
		2 TE	Proteins	$k = 0.01653$ (0.007215, 0.02585)	1.692	−1.299	15
			Lipids	$k = 0.002987$ (0.002448, 0.003525)	0.02257	0.04536	15
Korsmeyer–Peppas	$F(t) = k_{KP} \times t^n \times Q_0$	NT	Proteins	$k_{KP} = 0.6536$ (0.5267, 0.7848) $n = 0.2094$ (0.1422, 0.2811)	0.4533	0.8686	14
			Lipids	$k_{KP} = 0.07278$ (0.03213, 0.1202) $n = 0.3083$ (0.1265, 0.5468)	0.09387	0.5818	14
		CS	Proteins	$k_{KP} = 0.4655$ (0.3883, 0.5448) $n = 0.1558$ (0.09422, 0.2199)	0.1544	0.8614	14
			Lipids	$k_{KP} = 0.05405$ (0.01501, 0.1009) $n = 0.2416$ (0.0005, 0.6102)	0.05685	0.3263	14
		1.5K	Proteins	$k_{KP} = 0.3552$ (0.2610, 0.4528) $n = 0.1362$ (0.03556, 0.2426)	0.2347	0.6733	14
			Lipids	$k_{KP} = 0.04685$ (0.008132, 0.1050) $n = 0.4678$ (0.1971, 0.9455)	0.1052	0.5613	14
		2K	Proteins	$k_{KP} = 0.49$ (0.4327, 0.5478) $n = 0.05314$ (0.003064, 0.1034)	0.07637	0.8726	14
			Lipids	$k_{KP} = 0.1089$ (0.06886, 0.1514) $n = 0.1781$ (0.004445, 0.3272)	0.04514	0.5855	14
		1.5 TE	Proteins	$k_{KP} = 0.5247$ (0.4192, 0.6332) $n = 0.1633$ (0.08978, 0.2408)	0.294	0.816	14
			Lipids	$k_{KP} = 0.06579$ (0.02265, 0.1178) $n = 0.3079$ (0.08965, 0.6144)	0.06792	0.4719	13
		2 TE	Proteins	$k_{KP} = 0.3614$ (0.2726, 0.4531) $n = 0.1447$ (0.05238, 0.2425)	0.2046	0.722	14
			Lipids	$k_{KP} = 0.02244$ (0.008779, 0.04011) $n = 0.4507$ (0.2642, 0.7115)	0.01174	0.7157	14

decellularized and NT samples, nor among samples treated with different concentrations of the same decellularization agent. These findings also indicate that the structural integrity of the dermal collagen network was preserved during processing.

Finally, the water-absorption capacity of dermis samples, an indicator of their ability to retain wound exudate, was evaluated using a rehydration test (Fig. 1F). All scaffolds demonstrated rapid swelling, reaching up to 400% of their dry weight after 3 min of soaking. Decellularized scaffolds exhibited significantly greater water uptake than NT samples ($p < 0.05$), with no notable differences among the decellularization protocols.

3.2. Biological evaluation and cell-scaffold interactions of decellularized dermis

Next, the biological properties of the freeze-dried dermis scaffolds were assessed. The viability and proliferative capacity of fibroblasts seeded onto the decellularized scaffolds were assessed using the MTT assay (Fig. 2A). All scaffolds supported cell proliferation for up to 15 days, except for the CS-treated group, which exhibited significantly lower proliferation, likely due to SDS in the CS protocol, a known cytotoxic agent that is difficult to remove thoroughly during rinsing. Accordingly, H&E staining confirmed successful colonization on all scaffolds, while the CS-treated group displayed markedly reduced and less organized cellular infiltration (Fig. 2B). The ECM was preserved across all treatment groups, with distinguishable macromolecular protein fibres, confirming the overall structural integrity. Nonetheless, qualitative differences in morphology were evident between protocols. Scaffolds treated with 1.5TE and 1.5K displayed denser, more compact fibre networks, suggesting a relatively mild impact on ECM organization. In contrast, the CS-treated scaffold exhibited the lowest fibre density, consistent with a more aggressive effect on the ECM structure. SEM and confocal imaging further demonstrated that fibroblasts adhered to the scaffold surfaces with an elongated morphology, aligning along the fibre orientation, which reflects their adaptation to the underlying architecture (Fig. 2C and D). Cells also exhibited a well-spread morphology without a consistent directional bias, highlighting favorable scaffold biocompatibility. Collectively, these findings demonstrate that, while all protocols preserved the fundamental ECM framework, confirming observations made with SEM and confocal imaging, they differentially influenced fiber density and organization, which, in turn, shaped cell-matrix interactions.

3.3. Integration of lyosecretome into dermis scaffolds and biological evaluation

Following characterization and validation of the dermis scaffolds' biological properties, they were integrated with MSC-secretome and

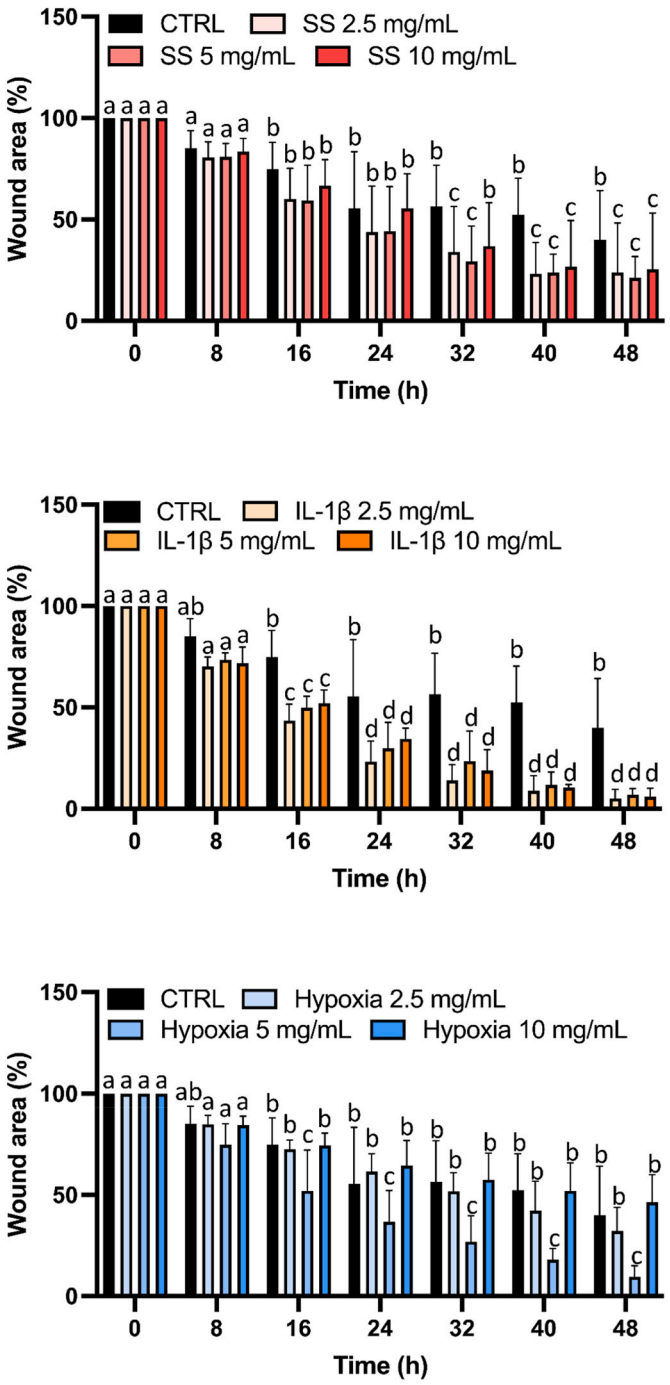

Fig. 4. Wound area (%) reduction of fibroblasts as a function of time and treatment. Different letters (a, b, c, and d) denote statistically significant differences between groups ($p < 0.05$); identical letters indicate no significant difference ($p > 0.05$). Data are presented as mean ± standard deviation. Statistical analysis was performed using a multifactor ANOVA and the LSD comparison test ($n = 3$).

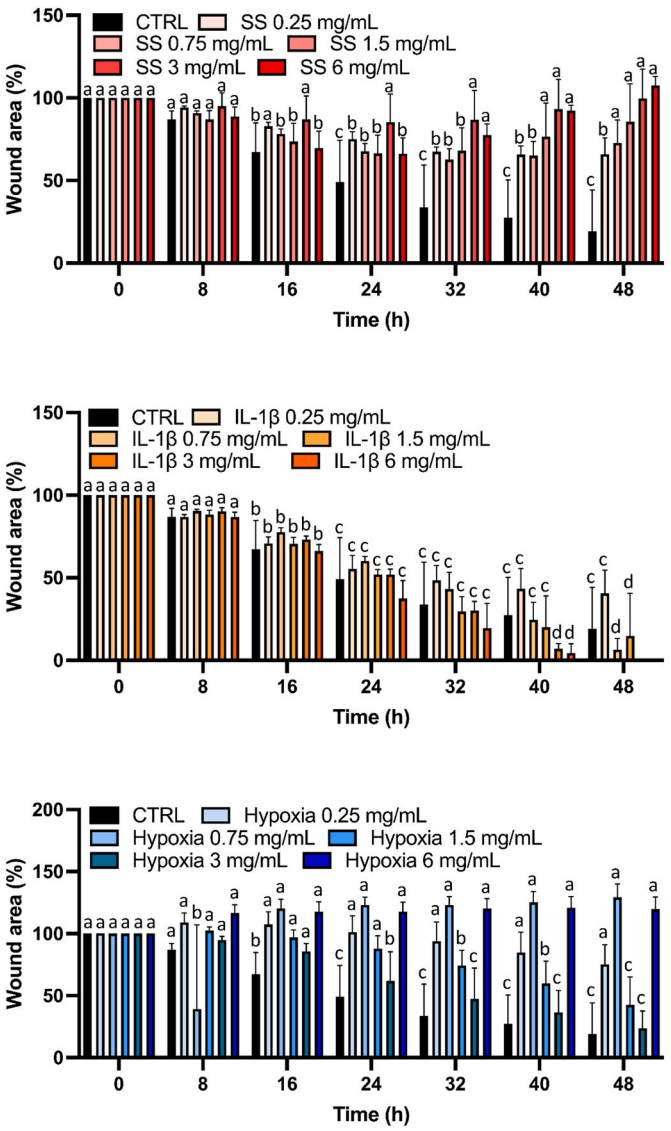

Fig. 5. Wound area (%) reduction of HUVECs as a function of time and treatment. Different letters (a, b, c, and d) denote statistically significant differences between groups ($p < 0.05$); identical letters indicate no significant difference ($p > 0.05$). Data are presented as mean ± standard deviation. Statistical analysis was performed using a multifactor ANOVA and the LSD comparison test ($n = 3$).

assessed for their potential as a delivery platform. The secretome was collected from MSCs stimulated with serum starvation alone or combined with IL-1β or hypoxia, and processed under GMP-compliant conditions into a ready-to-use, freeze-dried powder (lyosecretome). After lyophilization, protein and lipid content were quantified (Fig. 3A). Protein levels in the final lyosecretomes were comparable across conditions, consistent with the validated, Quality-by-Design manufacturing process, in which the ultrafiltration step is terminated at a pre-defined protein concentration target [46]; nonetheless, pre-standardization measurements showed that hypoxia-treated MSCs produced lower total protein than the other groups (Table S2). In contrast, lipid content, which is not standardized during processing, varied significantly, with lyosecretomes derived from IL-1β-stimulated or hypoxia-exposed MSCs showing a significant reduction in lipid levels ($p < 0.05$).

Lyosecretomes were then loaded onto both decellularized and NT freeze-dried dermis scaffolds via passive absorption, and release kinetics were assessed in PBS (Fig. 3B). Protein release differed according to the decellularization protocol: NT scaffolds released nearly 60% of the loaded proteins, CS and 1.5TE samples released ~50%, while 2TE, 1.5K, and 2K scaffolds released <40%. These differences likely reflect variations in protein adsorption capacity, which is influenced by the scaffold's surface properties and composition. For example, the presence of residual cellular components in NT scaffolds may reduce protein adsorption by competing for binding sites, thereby increasing release, whereas structural and porosity changes introduced by decellularization modulate protein retention. By contrast, lipid release was rapid and nearly complete within 6 h across all scaffold types, consistent with the

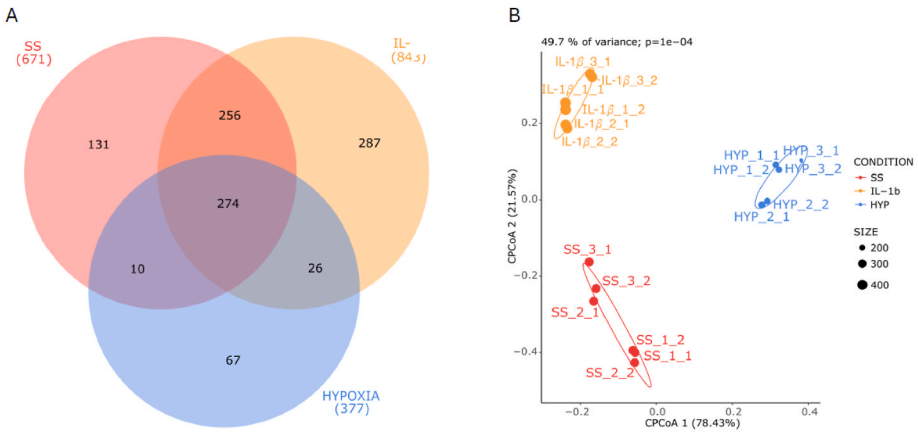

Fig. 6. Proteomic analysis of lyosecretomes. (**A**) Venn diagram of the total proteins identified (n = 1051) across the experimental conditions. (**B**) CPCoA showing sample clustering based on secretome protein composition: serum starvation (red), IL-1β (orange) and hypoxia (blue). (For interpretation of the references to color in this figure legend, the reader is referred to the Web version of this article.)

low affinity of lipid-based EVs for dermal matrix components, leading to minimal adsorption and faster dispersion into the surrounding medium.

The drug release data were further processed by elaborating on the release's kinetic model. Table 2 lists the results of the in vitro release model fitting for both proteins and lipids from dermis scaffolds. Protein release from dermis scaffolds is primarily governed by diffusion, as evidenced by fits to the Ritger-Peppas and Korsmeyer-Peppas models, with R^2 values near or above 0.8. However, the Peppas-Shalin model – designed to account for both Fickian diffusion (first term) and case-II relaxation or erosion (second term) – yielded inconclusive results, preventing definitive conclusions about the role of erosion in these systems [61,62]. Comparing protein diffusion across samples, decellularized scaffolds exhibited slower release rates than NT dermis, with k values ranging from 0.3552 to 0.5247 versus 0.6536 in NT dermis scaffolds. Lipid release showed a weaker fit to the Ritger-Peppas and Korsmeyer-Peppas models, with R^2 values around 0.5 or slightly above. Unlike proteins, lipid diffusion did not consistently differ between decellularized and NT dermis, as k values for decellularized samples (0.02244 to 0.1089) were similar to those of NT dermis (0.07278). The release exponent n in the Ritger-Peppas and Korsmeyer-Peppas equations was not analyzed, as these equations apply to systems with defined geometries (e.g., planar, cylindrical, or spherical) that do not reflect the irregular structures of the dermis used in this study.

The scratch assay, performed on GFP-expressing fibroblasts (Fig. 4) and HUVECs (Fig. 5), was used to evaluate the wound-healing potential of lyosecretomes derived from different stimulating conditions. In fibroblasts, the untreated control (CTRL) showed only a partial reduction in wound area over time, decreasing to 62.5% after 24 h and 45.1% after 48 h. Lyosecretome obtained from serum-starved MSCs promoted wound closure in a time-dependent ($p < 0.05$) but not dose-dependent ($p > 0.05$) manner, with wound areas at 32, 40, and 48 h significantly smaller than those of the control at the same time points. Treatment with lyosecretome derived from MSCs exposed to IL-1β further enhanced wound healing, with significant reductions in wound area observed as early as 16 h ($p < 0.05$), again without a dose-dependent effect ($p > 0.05$). In contrast, lyosecretome from hypoxia-stimulated MSCs did not improve wound closure compared to the control at most concentrations, except at 5 mg/mL, where significant decreases in wound area were detected at 16, 24, 32, 40, and 48 h ($p < 0.05$) (Fig. 4). In HUVECs, treatment with lyosecretome derived from MSCs stimulated with IL-1β did not impair wound closure compared to the control, although no significant enhancement was observed except at the highest concentrations tested (3 and 6 mg/mL) after 40 and 48 h. Conversely, lyosecretome from serum-starved MSCs significantly hindered wound closure relative to the control ($p < 0.05$), particularly at higher concentrations (3 and 6 mg/mL), where wound areas remained larger throughout the observation period. Similarly, lyosecretome derived from hypoxia-stimulated MSCs markedly delayed wound healing at all concentrations tested, except at 3 mg/mL, for which the wound area reduction at 32, 40, and 48 h was not significantly different from the control ($p > 0.05$) (Fig. 5).

3.4. *Characterization of wound healing-related proteins in stimulated MSC-lyosecretomes*

The lyosecretome obtained from different stimulations (serum starvation alone or combined with IL-1β or hypoxia) was finally analyzed by high-throughput proteomics to shed light on signatures involved in wound repair. Three biological replicates per condition were analyzed in two technical replicates, resulting in a total of 18 LC-MS/MS runs; all replicates demonstrated good repeatability, as further supported by Spearman's correlation coefficients (Fig. S1). A total of 1051 distinct proteins were identified, and about 26% (274 proteins) were found in all conditions (Table S3). The differences between the examined conditions were highlighted in a Venn diagram showing the number of shared and group-specific proteins (Fig. 6A); it illustrates a partial overlap in protein composition among the three different secretomes. In contrast, 131, 287, and 67 proteins were identified explicitly in serum starvation, IL-1β, and hypoxic conditions, respectively, suggesting a secretome-specific modulation. This clue was confirmed through CPCoA (Fig. 6B): principal component 1 (CPCoA1), accounting for 78% of the total variance, distinctly separated the serum starvation and IL-1β secretomes from the hypoxia one, while CPCoA2 (21% of the variance) differentiated the serum starvation group from the others.

To estimate a ranking of the most abundant proteins per condition, PSM values were normalized based on MW, as reported in section 2.6.3. Although most proteins were detected across all conditions, some of them showed marked quantitative differences in quantification. In this scenario, the serum-starved secretome showed elevated levels of pentraxin-related protein 3 (PTX3), SPARC, and Tropomyosin β chain (TPM2). IL-1β stimulation markedly increased the expression of proteins, including T cell receptor alpha joining 56 (TRAJ56), metalloproteinase inhibitor 1 (TIMP1), 72 kDa type IV collagenase (MMP2), Stromelysin-1 (MMP3), and Plasminogen activator inhibitor 1 (SERPINE1) (Table 3). Instead, the hypoxic condition was characterized by higher levels of albumin (ALB), alpha-2-HS-glycoprotein (AHSG), actin alpha cardiac muscle 1 (ACTC1), hemoglobin subunit alpha (HBA1), and keratins (Table 3).

In agreement with the scratch test, a preliminary functional analysis revealed the enrichment of pathways associated with wound healing.

Table 3
Rank list of the 20 most abundant proteins in secretomes from MSCs cultured in serum starvation alone or combined with IL-1β or hypoxia. The normalized PSMs were obtained following the formula (PSMs/MW)*110, where MW is the molecular weight of a given protein and 110 represents the aminoacidic average molecular weight; IF = identification frequency (n = 6 per condition). For each condition, the first 20 ranked proteins (by quantity) are shown in brackets.

Gene name	nPSMs			IF (n = 6)		
	Serum starvation	IL-1β	Hypoxia	Serum starvation	IL-1β	Hypoxia
TRAJ56	66.0 (13)	495.0 (1)	156.8 (2)	2	5	4
ALB	352.3 (1)	331.4 (2)	472.6 (1)	6	6	6
FN1	213.5 (2)	290.9 (3)	47.3 (12)	6	6	6
TIMP1	107.2 (5)	198.8 (4)	34.6	6	6	6
VIM	109.7 (4)	192.4 (5)	74.2 (6)	6	6	6
MMP2	73.2 (10)	142.4 (6)	7.2	6	6	4
SERPINE1	76.9 (9)	131.8 (7)	28.9	6	6	6
ACTB	83.0 (8)	118.2 (8)	94.9 (4)	6	6	6
MMP3	21.1	115.8 (9)	0.0	6	6	0
KRT1	22.2	106.0 (10)	132.7 (3)	6	6	6
COL1A2	85.9 (6)	103.6 (11)	10.5	6	6	6
TPI1	48.1 (19)	101.1 (12)	39.2 (19)	6	6	6
COL1A1	84.9 (7)	90.4 (13)	9.9	6	6	6
DCN	57.2 (16)	86.7 (14)	8.8	6	6	4
PTX3	117.1 (3)	76.9 (15)	43.7 (15)	6	6	6
BGN	38.7	76.1 (16)	1.3	6	6	3
CALU	66.2 (12)	75.6 (17)	33.1	6	6	6
PLOD1	26.1	73 (18)	1.5	6	6	2
P4HB	40.4	70.1 (19)	29.1	6	6	6
ANXA2	45.6 (20)	68.4 (20)	44.2 (14)	6	6	6
LUM	66.8 (11)	65.8	21.9	6	6	6
SPARC	62.5 (14)	54.0	18.0	6	6	6
TPM4	60.4 (15)	58.5	57.9 (11)	6	6	6
SERPINE2	55.0 (17)	54.2	7.9	6	6	4
TPM2	52.0 (18)	31.3	32.9	6	5	5
AHSG	25.6	19.1	74.6 (5)	5	6	6
KRT9	3.8	62	69.1 (7)	5	6	6
ACTC1	38.4	39.6	64.5 (8)	5	3	6
HBA1	34.9	28.8	62.5 (9)	5	6	6
KRT10	4.6	55.6	59.6 (10)	6	6	6
KRT14	0.0	45.5	45.2 (13)	0	6	6
KRT16	0.0	51.9	42.9 (16)	0	4	6
KRT2	3.9	45.9	41.5 (17)	3	6	6
TMSB4X	43.5	65.3	39.9 (18)	5	6	5
LDHA	39.5	64.0	37.5 (20)	6	6	6

Specifically, "complement activation", "intermediate filament organization", "regulation of extracellular matrix organization", and "vasculature development" were enriched in serum starvation and IL-1β secretomes (Fig. S2). On this basis, proteins involved in wound healing were specifically investigated. Several of them, including decorin (DCN), fibronectin (FN1), collagens, and key regulators of extracellular matrix remodeling (MMPs and TIMPs), were among the most abundant (Table S3). Notably, they were globally most represented in IL-1β, correlating with its highest effectiveness in improving wound regeneration mechanisms (Figs. 4, 5, and 7A).

To delve deeper into the molecular player most likely involved in this process, a subset of 61 proteins annotated for wound-healing was selected (Table S4), transformed into a PPI network, and grouped into functional modules (Fig. 7B). Most factors were highly abundant in the IL-1β-stimulated secretome, fitting with a pronounced pro-regenerative action. Differently, their levels were markedly reduced under hypoxic stimulation, while the serum starvation condition exhibited an intermediate level.

4. Discussions

This study investigated the feasibility of developing an advanced wound-healing scaffold by combining decellularized dermis with lyosecretome – a standardized, freeze-dried MSC-secretome obtained through a scalable, GMP-compliant manufacturing process [45,46]. Through leveraging both the preserved ECM architecture of dermis and the paracrine regenerative potency of the MSC-secretome, this approach was designed to overcome the well-recognized limitations of conventional wound therapies, including limited regenerative capacity, lack of structural support for cell infiltration, insufficient delivery of bioactive factors, and poor control of chronic inflammation [63,64]. In doing so, it addresses key barriers to chronic wound repair, including impaired cell proliferation, persistent inflammation, and delayed matrix remodeling.

To this end, dermis scaffolds were decellularized using five distinct protocols, producing acellular matrices that can provide structural support, retain moisture, and control the release of bioactive factors. DNA quantification and multiphoton imaging confirmed the effective removal of cellular material in all scaffolds, while preserving ECM integrity – a crucial requirement for maintaining scaffold bioactivity and avoiding immune rejection [65]. Structural analysis revealed protocol-dependent differences with important functional implications: the 1.5K protocol generated scaffolds with higher porosity and more uniform pore distribution, favoring fibroblast infiltration and nutrient diffusion [66,67] compared to the others, whereas TE-based protocols produced denser ECM networks that may better maintain mechanical strength but restrict cellular penetration [68,69]. The 2K protocol yielded a stratified collagen arrangement, whereas CS scaffolds, despite having a well-organized fibrillar network, were compromised by residual detergent toxicity, highlighting the need to balance ECM preservation with the removal of cytotoxic surfactants [70]. This difference in surfactant exposure also helps explain the comparatively higher FTIR-derived collagen and lipid signal retained in CS scaffolds: the shorter, sequential exposure (8 h per solution), combined with the lower ionic strength of the SDS-based step, appears less efficient at extracting lipids and solubilizing collagen than the more prolonged single-step TE/K protocols, despite achieving comparable DNA removal. Rehydration studies demonstrated that decellularized scaffolds absorbed substantially more water than NT dermis, reflecting their highly hydrophilic composition, primarily composed of glycosaminoglycans and proteoglycans, and larger inter-fibrillar gaps following cell removal [71]. This property enhances their ability to maintain a moist wound environment, a known facilitator of epithelial migration and granulation tissue formation [72].

Loading lyosecretomes onto the scaffolds further underscored the importance of ECM architecture in modulating paracrine factor release. Protein release was slower and less complete in decellularized scaffolds

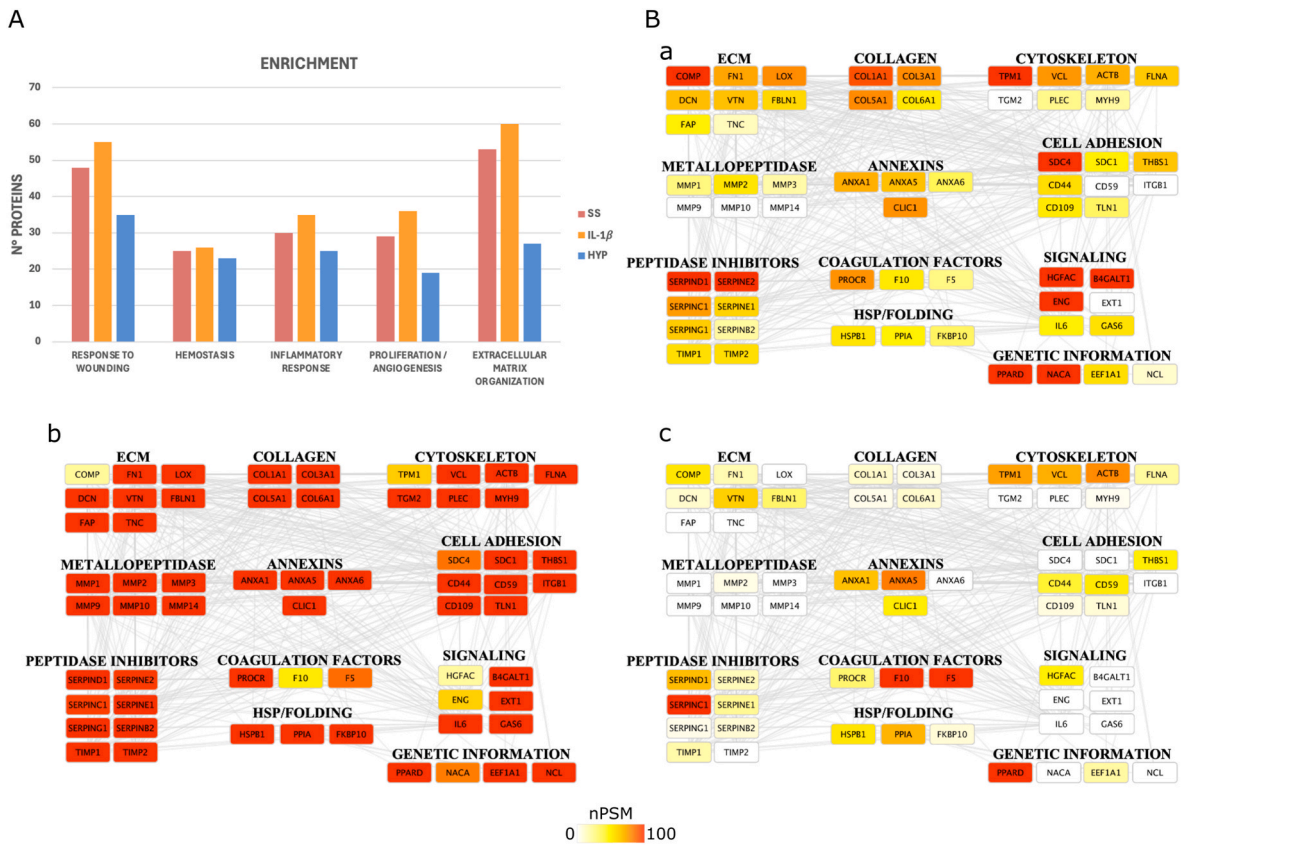

Fig. 7. **(A)** Enrichment in the wound healing process and its corresponding phases (hemostasis, inflammation, proliferation/angiogenesis, and extracellular matrix organization) starting from the number of proteins identified in serum-starved (SS), IL-1β, and hypoxic (Hyp) secretome. The enrichment was obtained using the STRING enrichment tool (FDR <0.05). (**B**) PPI network reconstructed by considering the proteins associated with the wound healing process in (a) serum starved, (b) IL-1β, and (c) hypoxic secretomes. The network was generated using Cytoscape's STRING APP, and proteins were grouped into functional modules based on their functions and families. Only experimentally annotated (score >0.15) and database-annotated (score >0.3) interactions were considered. Each node was color-coded based on PSM values normalized to a 0-100 scale (white = 0, yellow = 50, red = 100), and the corresponding chromatic scale was reported. (For interpretation of the references to color in this figure legend, the reader is referred to the Web version of this article.)

than in NT dermis, consistent with stronger protein adsorption to collagen fibers in decellularized dermis. Porous scaffolds, such as those produced by the 1.5K protocol, enabled more protein release, whereas denser matrices retained proteins for longer periods. In contrast, lipid release was rapid and largely scaffold-independent, reflecting distinct diffusion dynamics, with the notable exception of the 2TE scaffold, which showed slower and more limited lipid release. This protocol uses the highest surfactant concentrations among the TE-based methods, producing a denser, more compact collagen matrix; it thus can be hypothesized that the resulting reduction in pore size/connectivity increases tortuosity for lipid-vesicle diffusion through the matrix, slowing and reducing the extent of lipid release relative to the other scaffolds. Kinetic modeling confirmed that protein release followed diffusion-driven mechanisms, whereas lipid release did not conform to classical models, with the 2TE scaffold representing a partial exception, showing the highest R^2 among lipid fits (Ritger-Peppas, $R^2 = 0.7157$) and thus a release pattern closer to diffusion-controlled. Release studies were performed at pH 7.2; given that wound pH evolves during healing (from alkaline in chronic wounds toward neutral/acidic as healing progresses) and may influence protein adsorption to collagen and its subsequent release, testing release across this broader pH range represents a valuable direction for future work. Notably, scaffold loading required a second freeze-drying cycle for the lyosecretome. Previous work from our group showed that lyosecretome subjected to a comparable double freeze-drying process retains its wound-healing bioactivity in vivo [31], consistent with the functional activity observed here in the in vitro assays. A direct proteomic comparison of the lyosecretome before and after this second freeze-drying cycle was not performed in the present study and is planned as a future quality-control analysis.

Cytocompatibility was assessed through four complementary techniques – MTT viability, H&E histology, SEM, and confocal microscopy – which converged on a consistent picture of scaffold biocompatibility. All scaffolds except CS supported cell viability, proliferation, and adhesion, indicating that the preserved collagen framework provides a favorable microenvironment for fibroblast colonization. SEM and confocal imaging revealed that fibroblasts align along collagen fibers, highlighting the role of ECM architecture in guiding cellular organization [73] and function [74]. Integration with MSC-derived lyosecretome further enhanced scaffold therapeutic potential. MSCs were "educated" under serum starvation alone or in combination with hypoxia or pro-inflammatory cytokines (IL-1β), thereby tailoring the secretome composition for wound healing. For the freeze-dried products, the total protein levels appeared stable across conditions because the manufacturing process standardizes protein concentration during ultrafiltration. In contrast, lipid content varied because lipids were not normalized, specifically decreasing under IL-1β and hypoxia. Importantly, when examining unprocessed cell outputs, hypoxia preconditioning led to lower protein levels in equivalent cell populations, likely because low-oxygen exposure is known to suppress global translation through PERK-mediated eIF2α phosphorylation and mTOR signaling inhibition [75,76]. It was demonstrated that preconditioning MSCs can modulate the secretome composition also qualitatively, as well as its wound-healing potential, partially corroborating previous reports while also revealing context-dependent differences. Consistent

with the literature, the secretome from serum-starved-MSCs was enriched in ECM-associated proteins such as PTX3, SPARC, and TPM2, while IL1-β priming increased the secretion of matrix remodeling and wound repair factors, including TIMP1, MMP2, MMP3, and SERPINE1, consistent with the superior wound closure observed in fibroblast scratch assays and the maintained endothelial migration comparable to controls in HUVECs [77,78]. Hypoxic stimulation produced a cytoprotective secretome enriched in structural proteins like keratins and hemoglobin, in agreement with prior studies [79]; yet contrary to some reports, these hypoxia-derived MSC-secretomes showed minimal functional effect on wound closure in our assays, suggesting that the regenerative impact of hypoxia is highly context-dependent and influenced by cell type, culture conditions, and the functional readout used [79,80]. Additional studies using inflammatory cytokines or tissue-conditioned media have shown that the secretome can be further modulated to enhance angiogenesis or complex regenerative functions, highlighting the broader potential of preconditioning strategies [81]. As the HUVEC scratch assay reflects endothelial migration rather than angiogenic capacity per se, tube-formation assays – together with keratinocyte-based wound models – represent valuable additions for future studies to more directly assess the angiogenic and re-epithelialization potential of these lyosecretome-loaded scaffolds.

Overall, this combinatorial strategy addresses multiple pathophysiological hallmarks of chronic wounds, including impaired cell proliferation, excessive protease activity, and delayed ECM remodeling, while enabling controlled delivery of regenerative factors. The results provide a strong rationale for the development of a next-generation, off-the-shelf wound-healing device combining decellularized dermis with MSC-derived lyosecretome, offering a biologically relevant alternative to cell-based ATMPs.

5. Conclusions

This study demonstrates the feasibility of developing a next-generation wound-healing scaffold by integrating decellularized dermis with tailored mesenchymal stromal cell secretomes. All decellularization protocols effectively removed cellular components while preserving extracellular matrix structure, with differences in porosity and fiber organization influencing water absorption and secretome release. MSCs preconditioned through serum starvation alone or in combination with IL-1β or hypoxia secreted secretomes that exhibited distinct molecular profiles that supported specific regenerative functions, including matrix remodeling, extracellular matrix maintenance, and cytoprotection. When combined, the dermis scaffolds and secretomes from IL-1β-stimulated MSCs enhanced fibroblast wound closure in vitro, confirming biocompatibility and functional integration. These findings highlight how distinct microenvironmental stimuli can significantly influence the composition and functional potential of the MSC-secretome. In addition, they support the potential of this composite system as a ready-to-use, off-the-shelf strategy capable of addressing multiple barriers in chronic wound healing, providing a biologically active alternative to cell-based therapies.

CRediT authorship contribution statement

Marta Cecilia Tosca: Conceptualization, Investigation, Methodology. **Simona Turi:** Data curation, Investigation, Methodology, Writing – review & editing. **Dmitry Lim:** Methodology. **Angelo Modena:** Investigation, Writing – review & editing. **Edoardo Bertania:** Investigation, Writing – review & editing. **Elia Bari:** Conceptualization, Investigation, Methodology, Supervision, Visualization, Writing – original draft. **Lorena Segale:** Investigation. **Lorella Giovannelli:** Investigation. **Ivana Miletto:** Investigation. **Ilenia Rita Renzulli:** Investigation, Methodology, Software, Writing – review & editing. **Rossana Rossi:** Investigation, Methodology. **Pierluigi Mauri:** Investigation, Methodology. **Dario Di Silvestre:** Formal analysis, Investigation, Methodology, Writing – review & editing. **Giovanni Sesana:** Conceptualization, Supervision. **Maria Luisa Torre:** Conceptualization, Formal analysis.

Declaration of competing interest

M.L.T. is a co-founder and member of the company's advisory board Pharmaexceed S.r.l. This company had no role in the design of the study, in the collection, analysis, or interpretation of data, in the writing of the manuscript, or in the decision to publish the results.

Acknowledgements

The authors thank Alfatest, especially Dr. Marco Lorenzi, for the use of the Andor BC43 confocal microscope from Oxford Instruments. The authors also thank Dr. Simone Reano from CAAD - Centro Interdipartimentale "Centro di Eccellenza per la Ricerca traslazionale sulle Malattie Autoimmuni ed Allergiche", University of Piemonte Orientale, for assistance with multiphoton confocal microscopy.

Appendix A. Supplementary data

Supplementary data to this article can be found online at https://doi.org/10.1016/j.jddst.2026.108673.

Data availability

All data generated or analyzed during this study are included in the article or available from the corresponding author upon reasonable request. Raw images from the in vitro scratch wound-healing assays presented in this study (Section 2.5.2), together with the custom MATLAB® script used for wound area quantification, are included, among datasets from other studies, in a public Figshare collection freely available at: https://figshare.com/collections/2026_Bari_ScratchAssay/8477265. Proteomic data are available by ProteomeXchange Consortium repository at the site: ftp://massive-ftp.ucsd.edu/v13/MSV000102282/(accessed on 26/06/2026).

References

[1] C. Sen, Human wound and its burden: updated 2022 compendium of estimates, Adv. Wound Care 12 (2023) 657–670.
[2] S. Probst, C. Saini, G. Gschwind, A. Stefanelli, P. Bobbink, M. Pugliese, S. Cekic, D. Pastor, G. Gethin, Prevalence and incidence of venous leg ulcers-A systematic review and meta-analysis, Int. Wound J. 20 (2023) 3906–3921.
[3] K. Järbrink, G. Ni, H. Sönnergren, A. Schmidtchen, C. Pang, R. Bajpai, J. Car, Prevalence and incidence of chronic wounds and related complications: a protocol for a systematic review, Syst. Rev. 5 (2016).
[4] J. Guest, N. Ayoub, T. Mcilwraith, I. Uchegbu, A. Gerrish, D. Weidlich, K. Vowden, P. Vowden, Health economic burden that wounds impose on the national health service in the UK, BMJ Open 5 (2015).
[5] M. Olsson, K. Järbrink, U. Divakar, R. Bajpai, Z. Upton, A. Schmidtchen, J. Car, The humanistic and economic burden of chronic wounds: a systematic review, Wound Repair Regen. 27 (2019) 114–125.
[6] C. Sen, Human wound and its burden: updated 2020 compendium of estimates, Adv. Wound Care 10 (2021) 281–292.
[7] K. Bielefeld, S. Amini-Nik, B. Alman, Cutaneous wound healing: recruiting developmental pathways for regeneration, Cell. Mol. Life Sci. 70 (2013) 2059–2081.
[8] R.G. Frykberg, J. Banks, Challenges in the treatment of chronic wounds, Adv. Wound Care 4 (2015) 560–582.
[9] M. Millán-Reyes, D. Afanador-Restrepo, M. Carcelén-Fraile, A. Aibar-Almazán, M. Sánchez-Alcalá, J. Cano-Sánchez, M. Mesas-Aróstegui, Y. Castellote-Caballero, Reducing infections and improving healing in complex wounds: a systematic review and meta-analysis, J. Clin. Med. 14 (2025).
[10] C. Zhang, S. Zhang, B. Wu, K. Zou, H. Chen, Efficacy of different types of dressings on pressure injuries: systematic review and network meta-analysis, Nurs. Open 10 (2023) 5857–5867.
[11] K. Heyer, M. Augustin, K. Protz, K. Herberger, C. Spehr, S. Rustenbach, Effectiveness of advanced versus conventional wound dressings on healing of chronic wounds: systematic review and meta-analysis, Dermatology 226 (2013) 172–184.
[12] M.S. Chaudhry, A. Czekanski, In-situ bioprinting of skin- A review, Bioprinting 31 (2023) e00271.

[13] B. Sae, Wound treatment options. Wound Care Essentials, fifth ed. ed., Wolters Kluwer, Philadelphia, PA, 2020.
[14] L. Alrubaiy, K.K. Al-Rubaiy, Skin substitutes: a brief review of types and clinical applications, Oman Med. J. 24 (2009) 4–6.
[15] B. Magne, A. Demers, É. Savard, M. Lemire-Rondeau, N. Veillette, V. Pruneau, R. Guignard, A. Morissette, D. Larouche, F. Auger, L. Germain, Speeding up the production of clinical-grade skin substitutes using off-the-shelf decellularized self-assembled dermal matrices, Acta Biomater. 167 (2023) 249–259.
[16] C. Liu, M. Pei, Q. Li, Y. Zhang, Decellularized extracellular matrix mediates tissue construction and regeneration, Front. Med. 16 (2022) 56–82.
[17] A. Neishabouri, A. Khaboushan, F. Daghigh, A. Kajbafzadeh, M. Zolbin, Decellularization in tissue engineering and regenerative medicine: evaluation, modification, and application methods, Front. Bioeng. Biotechnol. 10 (2022).
[18] P. Crapo, T. Gilbert, S. Badylak, An overview of tissue and whole organ decellularization processes, Biomaterials 32 (2011) 3233–3243.
[19] R. Dutta, A. Dutta, Comprehension of ECM-cell dynamics: a prerequisite for tissue regeneration, Biotechnol. Adv. 28 (2010) 764–769.
[20] B. Dzamba, D. DeSimone, Extracellular matrix (ECM) and the sculpting of embryonic tissues, in: EXTRACELLULAR MATRIX AND EGG COATS, 2018, pp. 245–274.
[21] M. Barajaa, D. Ghosh, C. Laurencin, Decellularized Extracellular Matrix-Derived Hydrogels: a Powerful Class of Biomaterials for Skeletal Muscle Regenerative Engineering Applications, REGENERATIVE ENGINEERING AND TRANSLATIONAL MEDICINE, 2023.
[22] A. Ebrahimi Sadrabadi, P. Baei, S. Hosseini, M. Baghaban Eslaminejad, Decellularized extracellular matrix as a potent natural biomaterial for regenerative medicine, Adv. Exp. Med. Biol. 1341 (2021) 27–43.
[23] M. Bohác, L. Danisovic, J. Koller, J. Dragúnová, I. Varga, What happens to an acellular dermal matrix after implantation in the human body? A histological and electron microscopic study, Eur. J. Histochem. 62 (2018) 1–11.
[24] P. Milan, N. Lotfibakhshaiesh, M. Joghataie, J. Ai, A. Pazouki, D. Kaplan, S. Kargozar, N. Amini, M. Hamblin, M. Mozafari, A. Samadikuchaksaraei, Accelerated wound healing in a diabetic rat model using decellularized dermal matrix and human umbilical cord perivascular cells, Acta Biomater. 45 (2016) 234–246.
[25] J. Chu, P. Shi, X. Deng, Y. Jin, H. Liu, M. Chen, X. Han, H. Liu, Dynamic multiphoton imaging of acellular dermal matrix scaffolds seeded with mesenchymal stem cells in diabetic wound healing, J. Biophot. 11 (2018).
[26] S. Du, D. Zeugolis, T. O'Brien, Scaffold-based delivery of mesenchymal stromal cells to diabetic wounds, Stem Cell Res. Ther. 13 (2022).
[27] D. Ghetu, K. Raymond, I. Titorencu, M. Simionescu, Innovative strategies: use of stromal cell-derived secretome for chronic wound therapy, Int. J. Mol. Sci. 26 (2025).
[28] J. Huang, Q. Deng, L. Tsang, G. Chang, J. Guo, Y. Ruan, C. Wang, G. Li, H. Chan, X. Zhang, X. Jiang, Mesenchymal stem cells from perinatal tissues promote diabetic wound healing via PI3K/AKT activation, Stem Cell Res. Ther. 16 (2025).
[29] J. Prado-Yupanqui, L. Ramírez-Orrego, D. Cortez, V. Vera-Ponce, S. Chenet, J. Tejedo, R. Tapia-Limonchi, The hidden power of the secretome: therapeutic potential on wound healing and cell-free regenerative Medicine-A systematic review, Int. J. Mol. Sci. 26 (2025).
[30] N. Mussin, K. Zhilisbayeva, A. Baspakova, M. Kurmanalina, A. Tamadon, Umbrella review of mesenchymal stem cell-derived extracellular vesicles in preclinical models: therapeutic efficacy across diverse conditions, Front. Cell Dev. Biol. 13 (2025).
[31] E. Bari, D. Di Silvestre, L. Mastracci, F. Grillo, P. Grisoli, G. Marrubini, M. Nardini, M. Mastrogiacomo, M. Sorlini, R. Rossi, M.L. Torre, P. Mauri, G. Sesana, S. Perteghella, GMP-compliant sponge-like dressing containing MSC lyo-secretome: proteomic network of healing in a murine wound model, Eur. J. Pharm. Biopharm. 155 (2020) 37–48.
[32] R. Estrada, N. Li, H. Sarojini, J. An, M.-J. Lee, E. Wang, Secretome from mesenchymal stem cells induces angiogenesis via Cyr61, J. Cell. Physiol. 219 (2009) 563–571.
[33] S. Bartaula-Brevik, A.I. Bolstad, K. Mustafa, T.O. Pedersen, Secretome of mesenchymal stem cells grown in hypoxia accelerates wound healing and vessel Formation in vitro, Int. J. Stem Cell Res. Transplant 4 (1) (2017).
[34] B. Zhao, Y. Zhang, S. Han, W. Zhang, Q. Zhou, H. Guan, J. Liu, J. Shi, L. Su, D. Hu, Exosomes derived from human amniotic epithelial cells accelerate wound healing and inhibit scar formation, J. Mol. Histol. 48 (2017) 121–132.
[35] L. Wang, L. Hu, X. Zhou, Z. Xiong, C. Zhang, H.M.A. Shehada, B. Hu, J. Song, L. Chen, Exosomes secreted by human adipose mesenchymal stem cells promote scarless cutaneous repair by regulating extracellular matrix remodelling, Sci. Rep. 7 (2017).
[36] C. Wang, M. Wang, T. Xu, X. Zhang, C. Lin, W. Gao, H. Xu, B. Lei, C. Mao, Engineering bioactive self-healing antibacterial exosomes hydrogel for promoting chronic diabetic wound healing and complete skin regeneration, Theranostics 9 (2019) 65–76.
[37] A.d.F. Ferreira, P.d.S. Cunha, V.M. Carregal, P.d.C. da Silva, M.C. de Miranda, M. Kuranth-Lima, M.I. Abreu de Melo, C.C. Faria Faraco, J.L. Barbosa, F. Frezard, V. Resende, M.A. Rodrigues, A.M. de Goes, D.A. Gomes, Extracellular vesicles from adipose-derived mesenchymal stem/stromal cells accelerate migration and activate AKT pathway in human keratinocytes and fibroblasts independently of miR-205 activity, Stem Cell. Int. 2017 (2017) 9841035.
[38] R.R. Mohan, R. Tripathi, A. Sharma, P.R. Sinha, E.A. Giuliano, N.P. Hesemann, S. S. Chaurasia, Decorin antagonizes corneal fibroblast migration via caveolae-mediated endocytosis of epidermal growth factor receptor, Exp. Eye Res. 180 (2019) 200–207.
[39] M. Rodrigues, C.C. Yates, A. Nuschke, L. Griffith, A. Wells, The matrikine Tenascin-C protects multipotential stromal cells/mesenchymal stem cells from death cytokines such as FasL, Tissue Eng. 19 (2013) 1972–1983.
[40] W.Y. Jia, Z.Y. Yao, J.J. Zhao, Q.B. Guan, L. Gao, New perspectives of physiological and pathological functions of nucleolin (NCL), Life Sci. 186 (2017) 1–10.
[41] E. Bari, I. Ferrarotti, M.L. Torre, A.G. Corsico, S. Perteghella, Mesenchymal stem/stromal cell secretome for lung regeneration: the long way through "pharmaceuticalization" for the best formulation, J. Contr. Release 309 (2019) 11–24.
[42] E. Friedrich, S. Lanier, S. Niknam-Bienia, G. Arenas, D. Rajendran, J. Wertheim, R. Galiano, Residual sodium dodecyl sulfate in decellularized muscle matrices leads to fibroblast activation in vitro and foreign body response in vivo, J. Tissue Eng. Regen. Med. 12 (2018) E1704–E1715.
[43] A. Molnar, T. Lakat, A. Hosszu, B. Szebeni, A. Balogh, L. Orfi, A. Szabo, A. Fekete, J. Hodrea, Lyophilization and homogenization of biological samples improves reproducibility and reduces standard deviation in molecular biology techniques, Amino Acids 53 (2021) 917–928.
[44] E. Bari, S. Perteghella, G. Marrubini, M. Sorrenti, L. Catenacci, G. Tripodo, M. Mastrogiacomo, D. Mandracchia, A. Trapani, S. Farago, P. Gaetani, M.L. Torre, In vitro efficacy of silk sericin microparticles and platelet lysate for intervertebral disk regeneration, Int. J. Biol. Macromol. 118 (2018) 792–799.
[45] E. Bari, S. Perteghella, D. Di Silvestre, M. Sorlini, L. Catenacci, M. Sorrenti, G. Marrubini, R. Rossi, G. Tripodo, P. Mauri, M. Marazzi, M.L. Torre, Pilot production of mesenchymal stem/stromal freeze-dried secretome for cell-free regenerative nanomedicine: a validated GMP-compliant process, Cells 7 (2018).
[46] M. Mocchi, E. Bari, G. Marrubini, A.F. Bonda, S. Perteghella, F. Tartara, F. Cofano, G.d. Perna, L. Giovannelli, D. Mandracchia, M. Sorlini, D. Garbossa, M.L. Torre, L. Segale, Freeze-dried mesenchymal stem cell-secretome pharmaceuticalization: optimization of formulation and manufacturing process robustness, Pharmaceutics 13 (2021) 1129.
[47] M. Dominici, K. Le Blanc, I. Mueller, I. Slaper-Cortenbach, F.C. Marini, D.S. Krause, R.J. Deans, A. Keating, D.J. Prockop, E.M. Horwitz, Minimal criteria for defining multipotent mesenchymal stromal cells. The international society for cellular therapy position statement, Cytotherapy 8 (2006) 315–317.
[48] E. Bari, F. Scocozza, S. Perteghella, M. Sorlini, F. Auricchio, M.L. Torre, M. Conti, 3D bioprinted scaffolds containing mesenchymal stem/stromal lyosecretome: next generation controlled release device for bone regenerative medicine, Pharmaceutics 13 (2021) 515.
[49] E. Bari, G. Di Gravina, F. Scocozza, S. Perteghella, B. Frongia, S. Tengattini, L. Segale, M. Torre, M. Conti, Silk fibroin bioink for 3D printing in tissue regeneration: controlled release of MSC extracellular vesicles, Pharmaceutics 15 (2023).
[50] D. Caccavo, An overview on the mathematical modeling of hydrogels' behavior for drug delivery systems, Int. J. Pharm. 560 (2019) 175–190.
[51] D. Lim, A. Bertoli, M. Sorgato, F. Moccia, Generation and usage of aequorin lentiviral vectors for Ca2+ measurement in sub-cellular compartments of hard-to-transfect cells, Cell Calcium 59 (2016) 228–239.
[52] R. Adusumilli, P. Mallick, Data Conversion with Proteowizard Msconvert, 2017.
[53] J. Eng, A. Mccormack, J. Yates, AN approach to correlate tandem mass-spectral data of peptides with amino-acid-sequences in a protein database, J. Am. Soc. Mass Spectrom. 5 (1994) 976–989.
[54] D. Pierluigi Mauri, Gianni, Chapter 6 A proteomic approach to the analysis of RNA degradosome composition in Escherichia coli, in: RNA Turnover in Bacteria, Archaea and Organelles, Academic Press, 2008, pp. 99–117.
[55] D. Szklarczyk, K. Nastou, M. Koutrouli, R. Kirsch, F. Mehryary, R. Hachilif, D. Hu, M. Peluso, Q. Huang, T. Fang, N. Doncheva, S. Pyysalo, P. Bork, L. Jensen, C. von Mering, The STRING database in 2025: protein networks with directionality of regulation, Nucleic Acids Res. 53 (2024) D730–D737.
[56] N.T. Doncheva, J.H. Morris, J. Gorodkin, L.J. Jensen, Cytoscape StringApp: network analysis and visualization of proteomics data, J. Proteome Res. 18 (2019) 623–632.
[57] K. Forfang, B. Zimmermann, G. Kosa, A. Kohler, V. Shapaval, FTIR spectroscopy for evaluation and monitoring of lipid extraction efficiency for oleaginous fungi, PLoS One 12 (2017).
[58] I. Dreissig, S. Machill, R. Salzer, C. Krafft, Quantification of brain lipids by FTIR spectroscopy and partial least squares regression, Spectrochim. Acta Mol. Biomol. Spectrosc. 71 (2009) 2069–2075.
[59] S. Iswariya, P. Velswamy, T. Uma, Isolation and characterization of biocompatible collagen from the skin of puffer fish (Lagocephalus inermis), J. Polym. Environ. 26 (2018) 2086–2095.
[60] K. Lopez, S. Ravula, R. Pérez, C. Ayala, J. Losso, M. Janes, I. Warner, Hyaluronic acid-cellulose composites as patches for minimizing bacterial infections, ACS Omega 5 (2020) 4125–4132.
[61] N.A. Peppas, B. Narasimhan, Mathematical models in drug delivery: how modeling has shaped the way we design new drug delivery systems, J. Contr. Release 190 (2014) 75–81.
[62] N.A. Peppas, Analysis of fickian and NON-fickian drug release from polymers, Pharm. Acta Helv. 60 (1985) 110–111.
[63] V. Falanga, Wound healing and its impairment in the diabetic foot, Lancet (N. Am. Ed.) 366 (2005) 1736–1743.
[64] S. Guo, L.A. DiPietro, Factors affecting wound healing, J. Dent. Res. 89 (2010) 219–229.
[65] M. Wong, L. Griffiths, Immunogenicity in xenogeneic scaffold generation: antigen removal vs. decellularization, Acta Biomater. 10 (2014) 1806–1816.

[66] F. Mukasheva, L. Adilova, A. Dyussenbinov, B. Yernaimanova, M. Abilev, D. Akilbekova, Optimizing scaffold pore size for tissue engineering: insights across various tissue types, Front. Bioeng. Biotechnol. 12 (2024).
[67] Y. Wang, R. Xu, G. Luo, Q. Lei, Q. Shu, Z. Yao, H. Li, J. Zhou, J. Tan, S. Yang, R. Zhan, W. He, J. Wu, Biomimetic fibroblast-loaded artificial dermis with "sandwich" structure and designed gradient pore sizes promotes wound healing by favoring granulation tissue formation and wound re-epithelialization, Acta Biomater. 30 (2016) 246–257.
[68] S. van Helvert, C. Storm, P. Friedl, Mechanoreciprocity in cell migration, Nat. Cell Biol. 20 (2018) 8–20.
[69] K. Wolf, M. te Lindert, M. Krause, S. Alexander, J. te Riet, A. Willis, R. Hoffman, C. Figdor, S. Weiss, P. Friedl, Physical limits of cell migration: control by ECM space and nuclear deformation and tuning by proteolysis and traction force, J. Cell Biol. 201 (2013) 1069–1084.
[70] J. Noro, H. Vilaça-Faria, R. Reis, R. Pirraco, Extracellular matrix-derived materials for tissue engineering and regenerative medicine: a journey from isolation to characterization and application, Bioact. Mater. 34 (2024) 494–519.
[71] Y. Zhang, T. Iwata, K. Nam, T. Kimura, P. Wu, N. Nakamura, Y. Hashimoto, A. Kishida, Water absorption by decellularized dermis, Heliyon 4 (2018) e00600.
[72] J.P. Junker, R.A. Kamel, E. Caterson, E. Eriksson, Clinical impact upon wound healing and inflammation in moist, wet, and dry environments, Adv. Wound Care 2 (2013) 348–356.
[73] F. Zhao, M. Zhang, M. Nizamoglu, H. Kaper, L. Brouwer, T. Borghuis, J. Burgess, M. Harmsen, P. Sharma, Fibroblast alignment and matrix remodeling induced by a stiffness gradient in a skin-derived extracellular matrix hydrogel, Acta Biomater. 182 (2024) 67–80.
[74] B. Seo, X. Chen, L. Ling, Y. Song, A. Shimpi, S. Choi, J. Gonzalez, J. Sapudom, K. Wang, R. Eguiluz, D. Gourdon, V. Shenoy, C. Fischbach, Collagen microarchitecture mechanically controls myofibroblast differentiation, Proc. Natl. Acad. Sci. USA 117 (2020) 11387–11398.
[75] H. Harding, I. Novoa, Y. Zhang, H. Zeng, R. Wek, M. Schapira, D. Ron, Regulated translation initiation controls stress-induced gene expression in Mammalian cells, Mol. Cell 6 (2000) 1099–1108.
[76] C. Koumenis, C. Naczki, M. Koritzinsky, S. Rastani, A. Diehl, N. Sonenberg, A. Koromilas, B. Wouters, Regulation of protein synthesis by hypoxia via activation of the endoplasmic reticulum kinase PERK and phosphorylation of the translation initiation factor eIF2α, Mol. Cell Biol. 22 (2002) 7405–7416.
[77] J. Riedl, C. Popp, C. Eide, C. Ebens, J. Tolar, Mesenchymal stromal cells in wound healing applications: role of the secretome, targeted delivery and impact on recessive dystrophic epidermolysis bullosa treatment, Cytotherapy 23 (2021) 961–973.
[78] J. Joshi, S. Verma, R. Upadhya, S. Bhat, R. Seetharam, Inflammatory priming of mesenchymal stromal cells enhances its secretome potential through secretion of anti-inflammatory and ECM modulating factors: insights into proteomic and functional properties, Biochem. Biophys. Res. Commun. 778 (2025).
[79] Y. Yang, Y. Wu, D. Yang, S. Neo, N. Kadir, D. Goh, J. Tan, V. Denslin, E. Lee, Z. Yang, Secretive derived from hypoxia preconditioned mesenchymal stem cells promote cartilage regeneration and mitigate joint inflammation via extracellular vesicles, Bioact. Mater. 27 (2023) 98–112.
[80] S. Wang, F. Umrath, W. Cen, A. Salgado, S. Reinert, D. Alexander, Pre-conditioning with IFN-γ and hypoxia enhances the angiogenic potential of iPSC-Derived MSC secretome, Cells (2022) 11.
[81] S. Wangler, A. Kamali, C. Wapp, K. Wuertz-Kozak, S. Häckel, C. Fortes, L. Benneker, L. Haglund, R. Richards, M. Alini, M. Peroglio, S. Grad, Uncovering the secretome of mesenchymal stromal cells exposed to healthy, traumatic, and degenerative intervertebral discs: a proteomic analysis, Stem Cell Res. Ther. 12 (2021).